

EXTREME STAR FORMATION IN THE INTERACTING GALAXY ARP 299 (IC 694 + NGC 3690)^a

^aBASED ON OBSERVATIONS WITH THE NASA/ESA HUBBLE SPACE TELESCOPE, OBTAINED AT THE SPACE TELESCOPE SCIENCE INSTITUTE, WHICH IS OPERATED BY THE ASSOCIATION OF UNIVERSITIES FOR RESEARCH IN ASTRONOMY, INC. UNDER NASA CONTRACT NO. NAS5-26555. SOME OF THE OBSERVATIONS REPORTED IN THIS PAPER WERE OBTAINED WITH THE MULTIPLE MIRROR TELESCOPE, WHICH IS OPERATED JOINTLY BY THE SMITHSONIAN ASTROPHYSICAL OBSERVATORY AND THE UNIVERSITY OF ARIZONA.

ALMUDENA ALONSO-HERRERO, GEORGE H. RIEKE, MARCIA J. RIEKE

Steward Observatory, The University of Arizona, Tucson, AZ 85721

AND

NICK Z. SCOVILLE

California Institute of Technology, Pasadena, CA 91125

Draft version February 5, 2020

ABSTRACT

We present a comprehensive study of the star-formation properties of the infrared luminous galaxy Arp 299 (IC 694 + NGC 3690). The observations include *HST*/NICMOS imaging and MMT optical and near-infrared spectroscopy together with *HST* archival data. We correct the galaxy parameters for extinction and use the results as boundary conditions for evolutionary starburst models.

These models and other arguments show that Arp 299 has been going through a broad variety of interaction-induced star formation for the last ~ 15 Myr. In addition to nuclear starbursts in the two colliding galaxies, there are nearby luminous star forming regions that may be the result of molecular clouds breaking up and starting to form massive stars as they approach the nuclear potential. Two regions near the interaction region have very recently formed massive stars (~ 4 Myr old). One of these regions in particular appears to have undergone a starburst of very short duration, in contrast with the 5-10 Myr durations that are typical of nuclear events. These regions will probably form gravitationally bound new dwarf galaxies, although they are close enough to the more massive original galaxies that they will probably eventually be subsumed into them. In addition, we find 19 H II regions at least as energetic as 30 Doradus, and 21 older star clusters that likely are the products of similar H II regions formed in the past. This population of supergiant H II regions is unprecedented in normal galaxies and emphasizes that the effects of the interaction propagate through the entire pair of galaxies.

Subject headings: Galaxies: individual (Arp 299, IC 694, NGC 3690) – galaxies: nuclei – galaxies: photometry – galaxies: stellar content – galaxies: interacting – infrared: galaxies

1. INTRODUCTION

Ultraluminous infrared galaxies that rival quasars in energy output were first identified nearly thirty years ago (Rieke & Low 1972), and were shown by *IRAS* fifteen years ago to exist in numbers comparable to those of quasars in the nearby Universe (e.g., Sanders et al. 1988). The exact nature of these extreme objects has been of great interest and debate since. Among the ultraluminous infrared class ($L_{\text{IR}} > 10^{12} L_{\odot}$) it is found that a large percentage are interacting/merging systems containing active galactic nuclei. The process of merging with accompanying super-starbursts appears to be an important stage in galaxy evolution, possibly even converting spiral galaxies into ellipticals. Sanders et al. (1988) suggested that the infrared luminous phase is the initial stage for the appearance of a quasar (see Sanders & Mirabel 1996 for a recent review).

To understand these objects requires observations at high physical resolution. However, because their space

density is low at the current epoch, there are few nearby examples where such resolution is possible. Arp 299 (NGC 3690/IC 694 or Mrk 171) is of high infrared luminosity ($L_{\text{IR}} = 5 \times 10^{11} L_{\odot}$), placing it among the luminous infrared galaxies, but also is one of the nearest examples of interacting starburst galaxies (distance $D = 42$ Mpc for $H_0 = 75 \text{ km s}^{-1} \text{ Mpc}^{-1}$).

Within Arp 299, a number of bright infrared and radio sources appear to be the regions of star formation and/or nuclear activity responsible for the large overall luminosity (see Gehrzi, Sramek, & Weedman 1983; Wynn-Williams et al. 1991 and references therein)¹. As in other luminous and ultraluminous galaxies, there is a high concentration of molecular hydrogen within relatively small regions around these sources. From CO maps, Sargent & Scoville (1991) estimated densities of molecular gas $\simeq 8 \times 10^5 M_{\odot} \text{ pc}^{-2}$ in IC 694, $\simeq 3 \times 10^4 M_{\odot} \text{ pc}^{-2}$ in components B1 and B2 of NGC 3690 and $\simeq 2 \times 10^4 M_{\odot} \text{ pc}^{-2}$ at the interface of both galaxies (region C+C'). These general characteris-

¹We use the notation introduced by Gehrzi et al. (1983) for the interacting pair of galaxies Arp 299: the nucleus of IC 694 (eastern component) is source A, and the sources in NGC 3690 (western component) are B1, B2, C and C' (see also Wynn-Williams et al. 1991 and Alonso-Herrero, Rieke, & Rieke 1998).

TABLE 1
LOG OF THE NICMOS OBSERVATIONS

Camera	Filter	t_{exp}	Field of view
NIC3	F164N	1024	51.2" \times 51.2" (IC 694+NGC 3690)
NIC3	F166N	1024	51.2" \times 51.2" (IC 694+NGC 3690)
NIC2	F160W	208	19.5" \times 19.5" (IC 694), 19.5" \times 19.5" (NGC 3690)
NIC2	F222M	528	19.5" \times 19.5" (IC 694), 19.5" \times 19.5" (NGC 3690)
NIC2	F237M	864	19.5" \times 19.5" (IC 694), 19.5" \times 19.5" (NGC 3690)
NIC2	F187N	320	19.5" \times 19.5" (IC 694), 19.5" \times 19.5" (NGC 3690)
NIC2	F190N	320	19.5" \times 19.5" (IC 694), 19.5" \times 19.5" (NGC 3690)
NIC2	F212N	2560	19.5" \times 19.5" (IC 694), 19.5" \times 19.5" (NGC 3690)
NIC2	F215N	2560	19.5" \times 19.5" (IC 694), 19.5" \times 19.5" (NGC 3690)
NIC1	F110M	256	42.6" \times 21.0" (IC 694 + NGC 3690) 8 image mosaic

tics are consistent with numerical simulations of collisions between gas-rich galaxies (see Barnes & Hernquist 1996 and references therein) that show how interactions lead to transportation of large quantities of molecular gas into the centers of galaxies. This concentration of gas leads to a strong burst of star-formation and may activate an AGN.

However, these properties make the centers of activity in luminous and ultraluminous infrared galaxies virtually impenetrable in the visible and ultraviolet. We report near infrared *HST*/NICMOS images that penetrate much of the interstellar extinction and are at an unprecedented level of resolution for this spectral region, up to 0.1" corresponding to 20 pc. We also use WFPC2 images of the system together with ground-based optical and infrared spectroscopy to derive the star formation history. These new data are placed in the context of the characteristics of the galaxy measured in other spectral regions, as summarized briefly in the preceding paragraph.

2. OBSERVATIONS

2.1. NICMOS observations

HST/NICMOS observations of Arp 299 were obtained on November 4 1997 using all three cameras. In Table 1 we give the log of observations, where column (2) is the filter, column (3) is the integration time and column (4) is the field of view of the images. The observations were obtained in a spiral dither with a 5.5 pixel spacing and with two, three or four positions. The plate scales for NIC1, NIC2 and NIC3 are 0.045" pixel $^{-1}$, 0.076" pixel $^{-1}$ and 0.20" pixel $^{-1}$ respectively.

The images were reduced with routines from the package *NicRed* (McLeod 1997). The main steps in the data reduction involve subtraction of the first readout, dark current subtraction on a readout-by-readout basis, correction for linearity and cosmic ray rejection (using fullfit), and flatfielding. Darks with sample sequences and exposure times corresponding to those of our observations were obtained from other programs close in time to ours. Usually between 10 and 20 darks were averaged together (after the subtraction of the first readout) for a given sample sequence. However, in the case of F110M we got better removal of the artifacts using a dark+sky image generated by median combining all the dithered galaxy images for this filter. Flatfield images were constructed from on-orbit data. Since our images were obtained after August 1997,

no correction for the pedestal effect was necessary. For more specific details on the reduction of the NIC3 images see Alonso-Herrero et al. (1998).

After removal of artifacts, the dithered galaxy images were registered to a common position using fractional pixel offsets and cubic spline interpolation, and combined to produce the final images. The NIC1 F110M images were mosaiced. Since there are no bright common sources in the overlapping regions of the images, we used the world coordinate information contained in the header to compute the offsets. All the NICMOS images were rotated to the usual orientation north up, east to the left.

Prior to flux-calibrating the images, we measured the background on blank corners of the images. Although this interacting pair of galaxies is known to be extended beyond the field of the NIC2 images, the background values measured in the NIC2 F222M filter image are in excellent agreement with the background measurements taken during the Servicing Mission Observatory Verification (SMOV) program. The flux calibration was performed using the conversion factors based on measurements of the standard star P330-E (Rieke 1999). The fully-reduced narrow-band images (NIC2 F187N, F190N, F212N and F215N, and NIC3 F164N and F166N) were first background subtracted, then flux calibrated, and finally shifted to a common position. The adjacent continuum image was subtracted from the corresponding line + continuum image to produce the final continuum-free line images.

Figure 1 shows the NIC3 F166N image of the pair of interacting galaxies. The NIC3 F166N filter at the redshift of Arp 299 contains the emission line [Fe II]1.644 μ m. The total field of view is 51.2" \times 51.2". The corresponding images of the continuum subtracted [Fe II]1.644 μ m line emission of the system can be found in Alonso-Herrero et al. (1998). Figure 2a and Figure 2b show both components through different filters as indicated in the figure caption. The field of view of all these images (except for the NIC1 F110M inset in Figure 2a) is 19.5" \times 19.5". The NIC2 F222M and F237M images are similar in morphology and are not shown here.

2.2. Optical and ultraviolet images from the *HST* archive

A Wide Field Planetary Camera 2 (WFPC2) image of Arp 299 was retrieved from the *HST* data archive. This

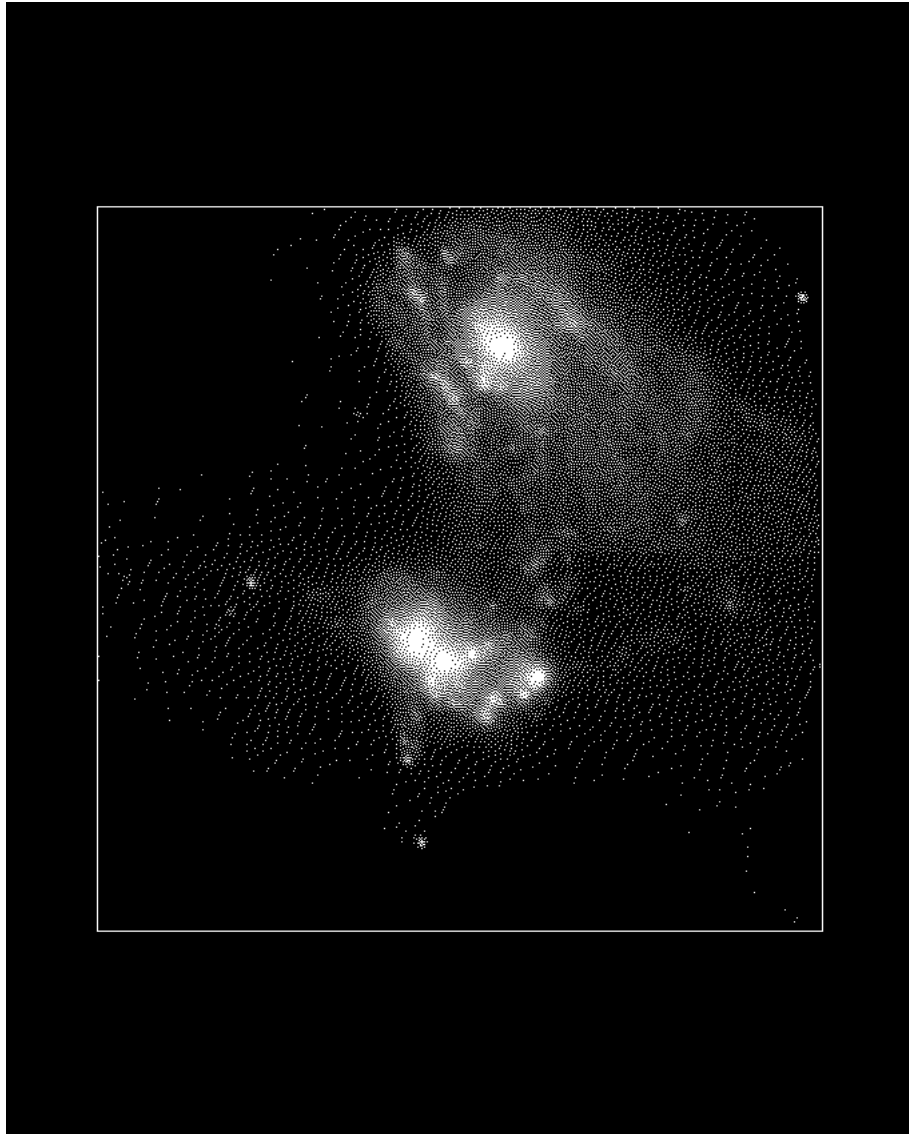


FIG. 1.— NIC3 F166N image ([Fe II]1.644 μ m + continuum) of the interacting system Arp 299 on a logarithmic scale. The total field of view is 51.2'' \times 51.2''. Orientation is north up, east to the left.

TABLE 2
LOW-RESOLUTION K -BAND INFRARED SPECTROSCOPY FOR A 1.2'' \times 1.2''
EXTRACTION APERTURE.

Source	$f(\text{H}_2)$ (erg cm $^{-2}$ s $^{-1}$)	EW(H ₂) (\AA)	$f(\text{Br}\gamma)$ (erg cm $^{-2}$ s $^{-1}$)	EW(Br γ) (\AA)	(CO) _{sp}	(CO) _{ph}
B1	9.52×10^{-15}	10.2	$8.56 \pm 0.5 \times 10^{-15}$	9.0 ± 0.5	0.14	0.07
B2	$< 2.4 \times 10^{-15}$	< 4	$< 3.1 \times 10^{-15}$	< 5	0.31	0.17
C	2.95×10^{-15}	5.1	$2.43 \pm 0.1 \times 10^{-14}$	41 ± 2

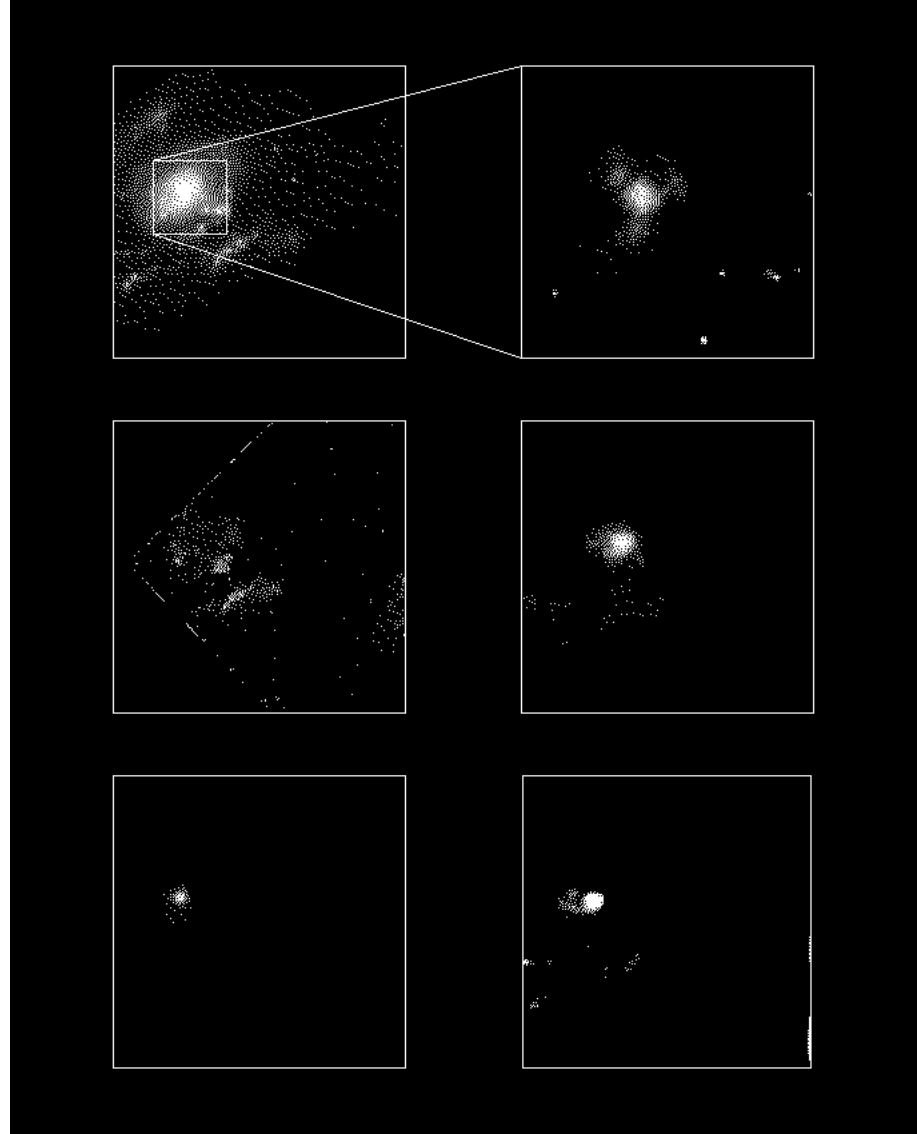


FIG. 2A.— IC 694. Top panels, left: NIC2 F160W (H -band continuum), and right: NIC1 F110M (continuum at $1.1 \mu\text{m}$) right. Middle panels, left: optical WFPC2 F606W, and right: continuum-subtracted NIC3 F166N ($[\text{Fe II}] 1.644 \mu\text{m}$). Bottom panels, left: continuum-subtracted NIC2 F215N (H_2 at $2.12 \mu\text{m}$), and right: continuum-subtracted NIC2 F190N ($\text{Pa}\alpha$). Orientation is north up, east to the left. The field of view of all the images except the inset is $19.5'' \times 19.5''$.

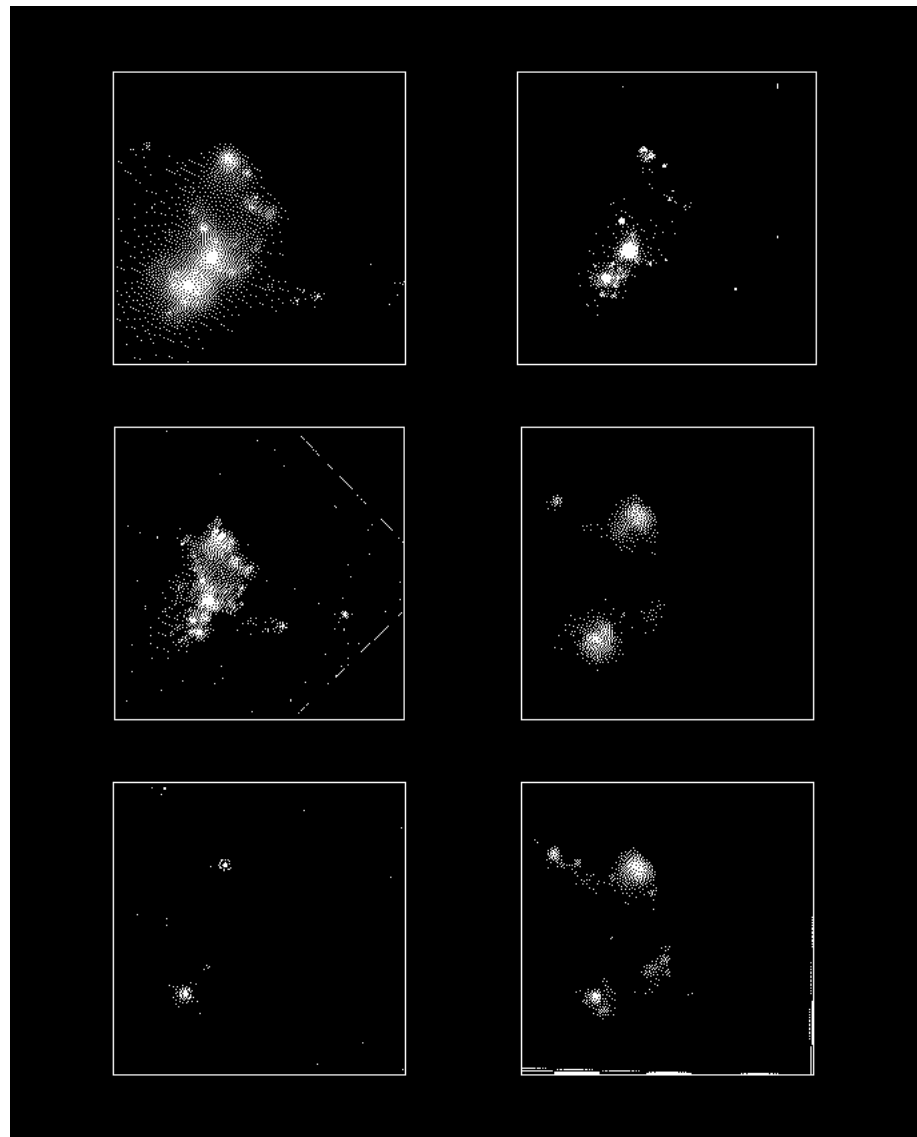


FIG. 2B.— Same as Figure 2a but for NGC 3690.

image was taken through the F606W filter on September 17 1994 with a total integration time of 500s and spatial sampling of $0.046''$ pixel $^{-1}$. Standard pipeline reduction procedures were applied. The image was rotated to the usual orientation north up, east to the left. Since a single integration was taken for this galaxy, the cosmic ray removal is problematic. The *cosmicray* task in IRAF successfully eliminated the most point-like hits but artifacts of extended hits remain in the data. The image is presented in Figure 2a and 2b, with the field of view matching that of NIC2.

We also retrieved UV FOC images from the *HST* archive for each of the components in the system, taken through the UV F220W filter with integration time of 897s for each component of the pair. Standard pipeline reduction procedures were used. Again the images were rotated to match the orientation of the NICMOS images. The plate scale of these images is $0.022''$ pixel $^{-1}$. The image of NGC 3690 was part of the study by Meurer et al. (1995) of the UV properties of starburst galaxies.

2.3. Ground-based H α imaging

CCD H α narrow-band images (on-line and off-line) of Arp 299 were obtained from the La Palma Observatory archive. The images were taken with the 1.5 m JKT telescope on January 21 1990 with a CCD-RCA2 detector. The integration time for the continuum+line and continuum images was 1,800s each. The reduction steps involved bias removal, dark current subtraction, and flat-fielding with both dome and sky flats. The plate scale of the images was $0.4''$ pixel $^{-1}$, providing a total field of view of $130'' \times 210''$.

Since no images of suitable standard stars are provided by the La Palma archive, the final continuum-subtracted H α image was calibrated with the spectroscopic data from Armus et al. (1989) and Gehrz et al. (1983). The latter reference provides fluxes through an effective aperture diameter of $5''$. The former authors provide the H α fluxes for components A and C of the interacting pair through a $2'' \times 4.5''$ aperture. Because of difficulties in setting the slit accurately on the heavily obscured sources, there are significant uncertainties in the line measurements. For example, Armus et al. (1989) report source C to have twice as much flux as source A, whereas our H α continuum-subtracted image indicates that source C is four times as bright as source A through the same aperture. Our flux calibration was based on an average of the values from the spectra; the effects of the uncertainties will be discussed when they are relevant to the analysis. In Figure 3 we present images of both the adjacent continuum and continuum-free H α line emission, showing the positions of the slits used for both the optical and near-infrared spectroscopy (Sections 2.4 and 2.5).

2.4. K-band spectroscopy

High ($\lambda/\Delta\lambda \simeq 3000$) and intermediate ($\lambda/\Delta\lambda \simeq 1000$) resolution spectra centered at wavelengths $2.32\,\mu\text{m}$ and $2.20\,\mu\text{m}$ respectively were obtained at the Multiple Mirror Telescope with the FSPEC infrared spectrometer (Williams et al. 1991) on February 11 and 12 1998. The slit size was $1.2'' \times 30''$ with plate scale $0.4''$ pixel $^{-1}$. The slit was centered on B1 at position angle PA = 145° to cover both sources B1 and B2, and at PA = 80° centered

on source C. The integration times were 96 minutes for sources B1 and B2, and 28 minutes for source C for the high-resolution data, and 14 minutes for each of the three sources for the low-resolution data.

Observations were obtained for each galaxy at three or four positions along the slit, integrating for 2 or 4 minutes at each position. Standard stars were measured in a similar fashion (using shorter integrations), interspersed with the galaxy observations. The standards were selected to be at similar air masses as the galaxies so they could be used to correct for atmospheric absorptions. The data reduction process involves dark current subtraction, flat-fielding, and sky subtraction. The correction for atmospheric absorption is performed by dividing the galaxy spectrum by the spectrum of a standard star observed at similar air mass. The resulting spectrum is multiplied by a solar spectrum to correct for the standard star absorption features. The wavelength calibration used OH sky lines from the list in Oliva & Origlia (1992).

We extracted spectra for B1, B2 and C with beam size $1.2'' \times 1.2''$. Since conditions were non-photometric, the flux calibration was performed for each source by extracting photometry with the same beam sizes on the NICMOS images taken through filters NIC2 F212N and NIC2 F222M. The continuum fluxes at $2.142\,\mu\text{m}$ (for the observed wavelength of H $_2$) and $2.188\,\mu\text{m}$ (for the observed wavelength of Br γ) were interpolated between these two filters. The line fluxes were computed by multiplying the observed equivalent width of the line by the continuum flux. Fluxes and equivalent widths for the Br γ and H $_2(1-0)S(1)$ emission lines are presented in Table 2.

Figures 4a and 4b show the fully-reduced spectra. To check the NICMOS photometry, we fitted the continuum slope between $2.22\,\mu\text{m}$ and $2.37\,\mu\text{m}$ using the NIC2 F222M and NIC2 F237M fluxes obtained for the corresponding apertures. The fits are shown in these figures as dashed lines; the agreement is very good. For the $^{12}\text{CO}(2, 0)$ band at $2.293\,\mu\text{m}$ we measure the spectroscopic index as defined in Kleinmann & Hall (1986), which is then transformed to a photometric CO index. Measurements of both indices for B1, B2 and C are given in Table 2. Source C does not show CO bands. Our values are in good agreement with Shier, Rieke, & Rieke (1996) and Vanzi, Alonso-Herrero, & Rieke (1998) for the components in common with both works.

2.5. Optical Spectroscopy

K. Luhman obtained optical spectra of NGC 3690 for us with the Red Channel Spectrograph at the Multiple Mirror Telescope on Mount Hopkins, on November 27–29 1997. He used the $270\,\text{g}\,\text{mm}^{-1}$ grating ($\lambda_{\text{blaze}} = 7300\,\text{\AA}$) to measure spectra from $4600\,\text{\AA}$ to $8600\,\text{\AA}$. A $2'' \times 180''$ slit with pixel size $0.6''$ pixel $^{-1}$ provided a spectral resolution of $\Delta\lambda = 18\,\text{\AA}$. To derive the sensitivity function of the array he also observed the standard star BD+8 2015. The 2-D spectra were subtracted from bias-subtracted frames, corrected for the sensitivity function and wavelength calibrated using He-Ar-Ne lamp spectra. We did not attempt to flux calibrate the data.

Spectra were extracted centered at B2 with position angles PA = 120° and PA = 145° , and centered near B1. Centering the slit on B1 with the acquisition camera proved

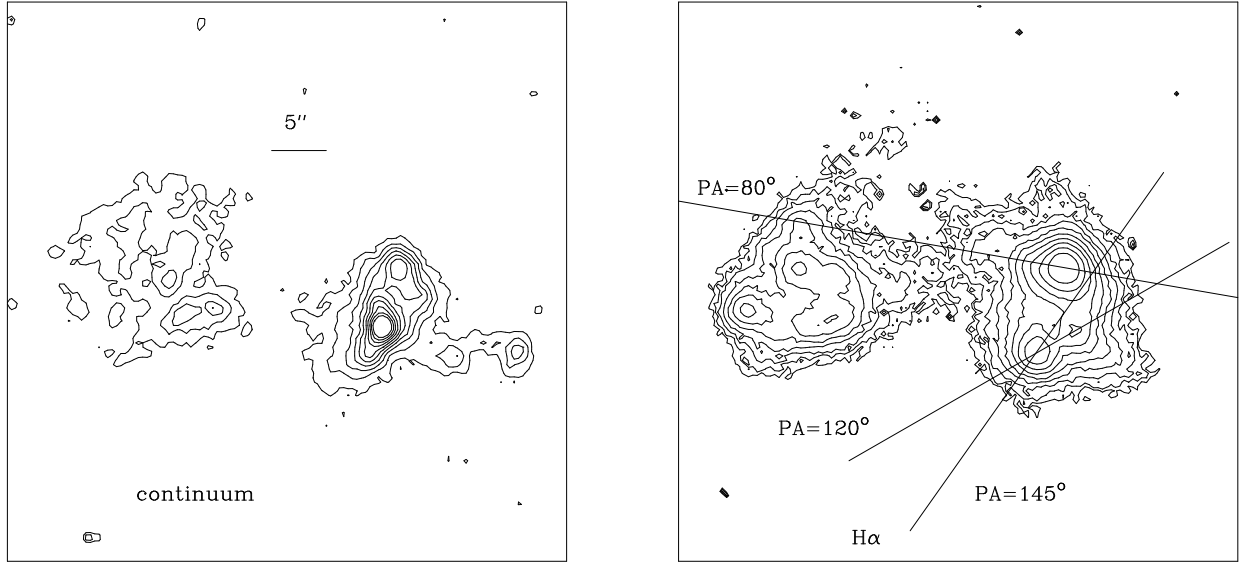


FIG. 3.— Contour plots on a linear scale of the continuum adjacent to H α (left panel) and continuum free H α line emission (right panel). The field of view (51'' \times 51'') and orientation match those of the NIC3 F166N image in presented in Figure 1.

TABLE 3
OPTICAL SPECTROSCOPY.

[O III]/H β	[O I]/H α	[N II]/H α	[S II]/H α	H α /H β	EW(H β)	EW(H α)
		Source B1 + B16?	$A_V = 4.2$ mag			
2.59	0.055	0.20	0.27	12.4	15	170
		Source B2	$A_V = 3.5$ mag			
1.27	0.020	0.34	0.21	9.8	5	55
		Source C	$A_V = 2.1$ mag			
1.42	0.018	0.35	0.17	6.0	93	607
		Source C'	$A_V = 2.1$ mag			
1.16	0.042	0.31	0.29	6.0	45	293
		Region north of A	$A_V = 2.9$ mag			
1.76	0.078	0.44	0.44	7.8	9	76
		H II region 6.6'' NW of B1	$A_V = 2.9$ mag			
1.57	0.013	0.34	0.19	7.6	48	300
		H II region 7.8'' NW of B1	$A_V = 2.1$ mag			
1.27	0.016	0.47	0.17	5.9	79	550
		H II region 4.8'' NW of B2	$A_V = 1.7$ mag			
1.16	0.016	0.34	0.21	5.2	45	277
		H II region 2.4'' NW of B2	$A_V = 1.9$ mag			
0.75	0.023	0.31	0.18	5.5	36	243

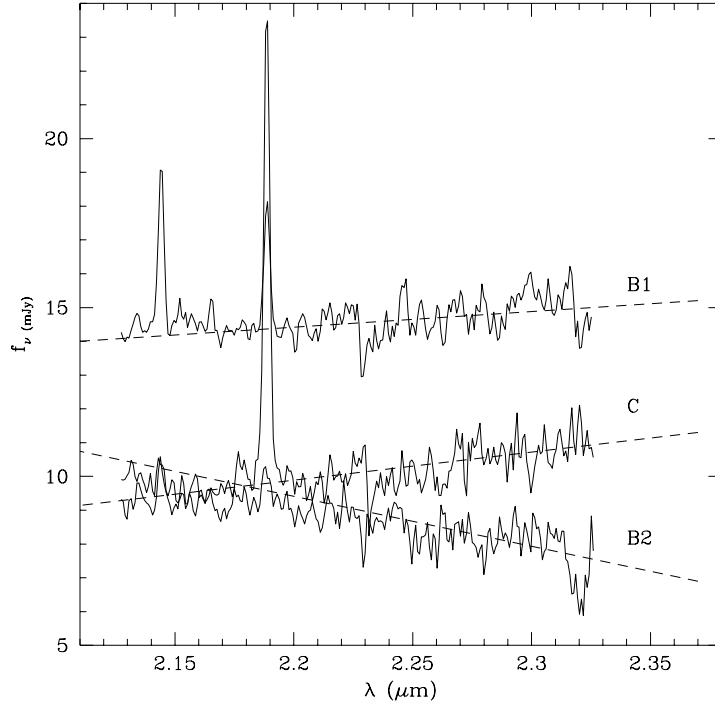


FIG. 4A.— Low resolution K -band spectroscopy for B1, B2 and C. The dashed lines show the linear fits to the continuum between $2.22 \mu\text{m}$ and $2.37 \mu\text{m}$ as measured through the NIC2 F222M and NIC2 F237M filters.

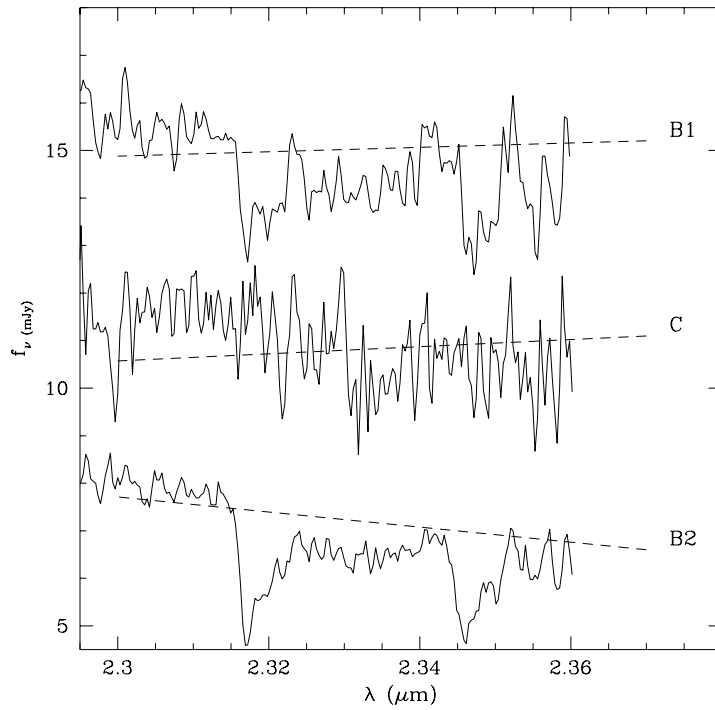


FIG. 4B.— Same as Figure 4a but for high resolution K -band spectroscopy.

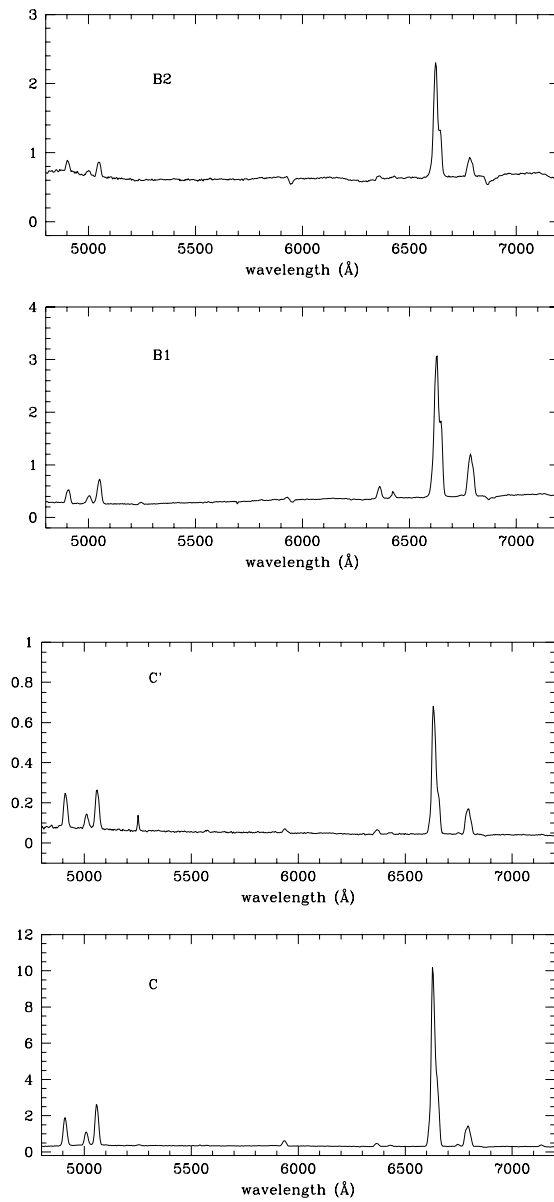


FIG. 5.— Optical spectra (in arbitrary units) for B1, B2, C, and C', along with a number of H II regions.

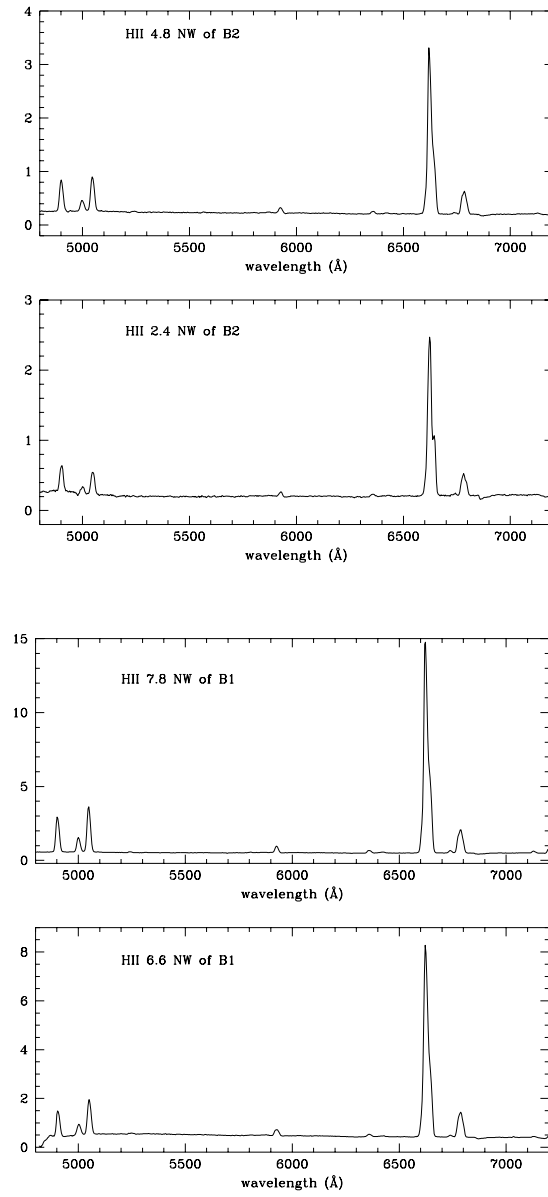


FIG. 5.— Continued.

difficult because this nucleus is barely seen in the optical. Therefore, the coordinates obtained from the NICMOS images were used, and the slit was kept at the same position angles as for B2. Finally the slit was centered at C with position angle PA= 80°. The position angles of the slits were chosen because PA= 145° includes B1 and B2, and PA= 120° includes the H II regions located northwest of B1. The spectrum centered at B1 probably contains the source B16 which is located $\simeq 1.5''$ southwest of B1 (see Section 3.1). The spectrum of B2 was extracted at the position of the peak of the continuum near H α . The spectrum centered at C at PA = 80° also contains C' and regions southwest of the nucleus of IC 694.

For extracting the 1-D spectra we used 3 pixel (1.8'') apertures. The positions of the slits and the regions for which we extracted spectra are shown in Figure 5. The fully reduced optical spectra (not calibrated in flux) are shown in Figures 5.a and 5.b for those regions for which we present line ratios and equivalent widths in Table 3. The optical line ratios of all the regions are consistent with those of H II as plotted in diagnostic diagrams such those in Ho, Filippenko, & Sargent al. (1993). The visual extinctions were computed from the Balmer decrement.

3. RESULTS

3.1. Continuum Morphology

Our NICMOS images of Arp 299 reveal an extremely complex morphology. Over the past few years it has been claimed that the nucleus of IC 694 could harbor an obscured AGN. An important result of the NICMOS imaging is that no dominant point-like source is seen anywhere in the system that would be a logical AGN candidate. The NIC1 F110M image (Figure 2.1) of IC 694 shows that the nucleus is resolved into at least three individual sources within a region of about 0.86'' ($\simeq 175$ pc) in diameter. These sources could be either young stellar clusters, or extinction shadows against a smooth source. Source B1 (see Figure 7b for identifications) in NGC 3690 appears to be extended at our resolution in the NIC1 F110M image, as does source B2. The curves of growth for sources B1, B2 and B21 for filter NIC1 F110M are shown in Figure 6 to illustrate that B2 is clearly extended, whereas B1 appears marginally extended. As comparison we plot the curve of growth of the source B21 which appears as a point source at our resolution. Sources B1 and B2 are also surrounded by a number of faint sources (see Figure 7b for identifications and Table 4 for the relative distances to either B1 or B2). Source C (which is seen as one source from the ground) is now resolved into 3 sources that we will refer to as C1, C2 and C3 (see Table 4 for relative positions). C1 and C2 are extended whereas C3 seems to be point-like at the resolution of the infrared images. The optical WFPC2 image, because of its higher spatial resolution, shows however that C3 is also extended. Additional sources are located southwest of the C complex (i.e., C4 and C5) and southeast of B1 (sources D1, D2, D3). The galaxy IC 694 also shows faint sources, most of them located along the spiral arms (probably H II regions), and labelled as A1, A2, A3, A4, A5 and A6 (Figure 7a). We can place an upper limit to the size of the unresolved sources from the NIC F110M image of 0.08'' (\simeq diffraction limit) or $\simeq 18$ pc for the assumed distance. However,

some of these faint sources appear to be slightly resolved in the WFPC2 image.

A comparison between the NICMOS images and the optical WFPC2 F606W image shows dramatically the effects of extinction. The latter image contains the H α emission line, so that low-extinction bright H II regions will show up in this filter. The most remarkable difference appears in the component IC 694. A careful alignment of the optical and near-infrared images to determine the position of the near-infrared peak on the optical image of IC 694 shows that the source (presumably the nucleus of the galaxy) is completely obscured in the optical (see Figure 2.a). The spiral arm southwest of A is clearly detected in the optical image. The WFPC2 image of NGC 3690 shows a closer correspondence with the near-infrared image than for IC 694, but still some differences are present. The very high spatial resolution of the WFPC2 image shows that both sources B1 and B2 are detected and extended (note the morphology of the ground-based continuum image near H α where the brightest source is B2, Figure 3), although B2 is much brighter than B1 at optical wavelengths (as already known from ground-based observations). Most of the faint sources seen in the NICMOS images (i.e., the B's, C's and D's sources) are also seen in the optical image, however some of them must be very obscured because they are very faint in the optical. On the other hand, source B16, which is barely seen in the NIC2 F160W image, appears to be almost as bright as B1 in the optical.

The effects of extinction are even more dramatic when the NICMOS images are compared with the ultraviolet FOC F220W image. We carefully cross-correlated the UV sources reported by Meurer et al. (1995, see their table 10), with the infrared ones, using relative coordinates. The brightest source in the UV image (NGC3690-1 in their notation) is identified with our source B21. The UV source NGC 3690-2 corresponds to B2. The double source NGC 3690-5 and NGC 3690-8 is located at the position of source B16, and therefore does not correspond to source B1 (as Meurer et al. 1995 indicated). Source B1 appears totally obscured at ultraviolet wavelengths. The positions of sources NGC 3690-6, NGC 3690-7, NGC 3690-9 and NGC 3690-10 are approximately consistent with those of C2, C3, C5 and C4 in our notation. Also noticeable is that the D complex is relatively bright in the UV, although it does not stand out in the IR. All the UV sources detected in NGC 3690 are embedded in a UV background which extends to greater radii than the individual sources. IC 694 is very faint in the ultraviolet image (not shown here) with only the southeast spiral arm and some very diffuse and faint emission near A.

These comparisons are a warning about the use of the UV to study starbursts, particularly ones that are less well resolved than Arp 299. The UV light can be dominated by lightly obscured regions that represent only a fraction of the true starburst region and which may be atypical of the integrated properties (e.g., the extended UV backgrounds in NGC 3690 and the relative suppression of IC 694).

3.2. Emission Line Morphology

The [Fe II]1.644 μ m and the Pa α continuum-subtracted images show bright emission from A, B1, and C (Figures 2.a and 2.b). From both these images it appears that very little line emission originates from source B2, confirm-

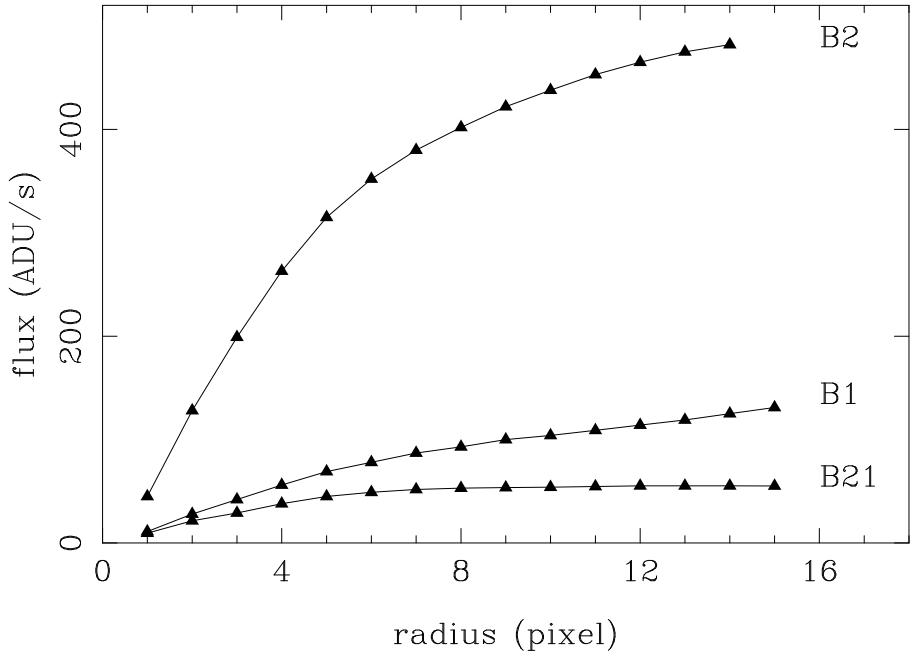


FIG. 6.— Curves of growth for sources B1, B2 and B21 for the NIC1 F110M filter.

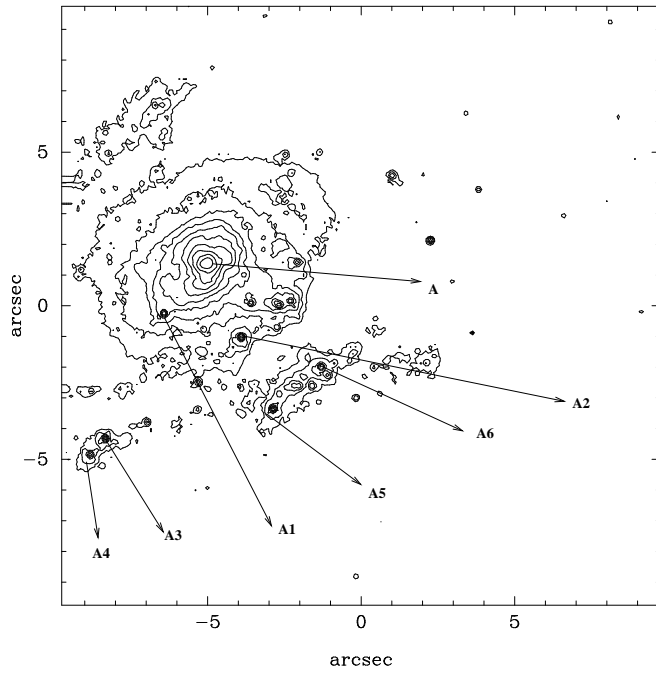


FIG. 7A.— Contour plot on a linear scale of the NIC2 F160W image of IC 694. We mark the positions of the A sources (Table 4). Orientation is north up, east to the left. The field of view is $19.5'' \times 19.5''$.

TABLE 4
PHOTOMETRY OF A, B1, B2, C1, AND FAINT SOURCES. RELATIVE DISTANCES AND FLUXES.

Source	ΔRA s	ΔDec "	$f(\text{F110M})$ mJy	$f(\text{F160W})$ mJy	$f(\text{F222M})$ mJy	$f(\text{F237M})$ mJy	$f(\text{F606W})$ erg cm $^{-2}$ s $^{-1}$ Å $^{-1}$
A	0	0	0.886	3.504	7.280	7.458	...
A1	0.17	-1.62	0.036	0.100	0.159	0.121	...
A2	-0.14	-2.39	0.057	0.124	0.129	0.097	...
A3	0.41	-5.70	0.047	0.086	0.097	0.075	...
A4	0.48	-6.20	0.023	0.063	0.073	0.058	...
A5	-0.27	-4.71	0.061	0.098	0.108	0.085	...
A6			0.050	0.079	0.080	0.057	...
B1	0.	0	0.824	2.909	10.739	13.827	0.19×10^{-15}
B11	0.04	-1.00	0.158	0.325	0.362	0.333	0.24×10^{-16}
B12	-0.08	-0.42	0.072	0.279	0.372
B13	-0.05	0.91	0.087	0.254	0.397	0.298	...
B14	-0.11	0.64	0.060	0.104
B15	0.09	0.83	0.044	0.115	0.138
B16	-0.06	-1.10	0.086	0.061	0.10×10^{-15}
B2	0	0	3.678	5.737	6.676	5.525	0.89×10^{-15}
B21	0.07	2.01	0.440	0.787	0.806	0.663	0.23×10^{-15}
B22	-0.17	-0.85	0.123	0.274	0.338	0.252	0.90×10^{-17}
B23	-0.03	1.14	0.088	0.173	0.152	0.127	0.18×10^{-16}
B24	-0.07	-0.77	0.054	0.091	0.093
B25	-0.30	-0.60	0.042	0.096	0.104	...	0.16×10^{-16}
B26	0.16	3.10	0.039	0.067	0.060	...	0.20×10^{-16}
C1	0	0	0.199	1.460	8.4071	11.152	0.72×10^{-16}
C2	-0.05	-0.31	0.171	0.255	0.22×10^{-15}
C3	-0.16	-1.00	0.199	0.307	0.307	0.206	0.76×10^{-16}
C4	-0.20	-3.25	0.119	0.224	0.208	0.154	0.51×10^{-16}
C5	-0.23	-2.63	0.051	0.084	0.083	...	0.32×10^{-16}
C'	0.68	0.77	...	0.081	0.165	0.160	...
D1	-1.09	-0.66	0.087	0.136	0.134	0.087	0.47×10^{-16}
D2	-0.96	-0.31	0.013	0.030	0.027
D3	-0.91	-0.94	0.031	0.048	0.046	...	0.10×10^{-16}

NOTE.—Relative distances for A1 through A6 are from A, relative distances for B11 through B16, and D1 through D3 are from B1, relative distances for B21 through B25 are from B2 and relative distances for C2 through C5 are from C1. The photometry for A, B1 and B2 is through a 0.9"-diameter photometry, whereas that of the faint sources is for a 0.5"-diameter aperture (corrected for aperture effects). Errors for the measured fluxes are 7% for the bright sources and 10% for the faint sources.

TABLE 5
OBSERVED H -BAND MAGNITUDES, COLORS AND (CO)_{NICMOS} INDEX.

Source	H	$J - H$	$H - K$	CO	$R - J$
A	13.724	1.330	1.361	-0.025	...
A1	17.588	1.073	1.039	0.239	...
A2	17.357	0.908	0.570	0.249	...
A3	17.746	0.807	0.649	0.229	...
A4	18.095	1.049	0.686	0.203	...
A5	17.614	0.720	0.632	0.209	...
A6	17.846	0.701	0.539	0.256	...
B1	13.927	1.230	2.061	-0.288	2.18
B11	16.305	0.880	0.638	0.079	2.38
B12	16.473	1.291	0.837
B13	16.575	1.108	1.019	0.249	...
B14	17.539	0.770
B15	17.430	1.034	0.720
B16	18.121	0.190	-0.15
B2	13.190	0.699	0.687	0.172	1.84
B21	15.347	0.788	0.548	0.178	1.15
B22	16.493	0.930	0.751	0.252	2.97
B23	16.991	0.853	0.386	0.165	2.09
B24	17.687	0.750	0.541
B25	17.636	0.939	0.618	...	1.57
B26	18.028	0.766	0.418	...	1.08
C1	14.676	1.705	2.646	-0.327	1.97
C2	16.570	0.672	0.13
C3	16.368	0.694	0.522	0.331	1.37
C4	16.712	0.823	0.443	0.259	1.34
C5	17.781	0.727	0.510	...	0.89
D1	17.253	0.703	0.505	0.352	1.04
D2	18.877	0.949	0.392
D3	18.372	0.699	0.462	...	1.55

NOTE.—Errors in the colors are ± 0.10 and ± 0.14 for the bright and faint sources respectively, whereas the errors associated with the (CO)_{NICMOS} are of the order of 20%.

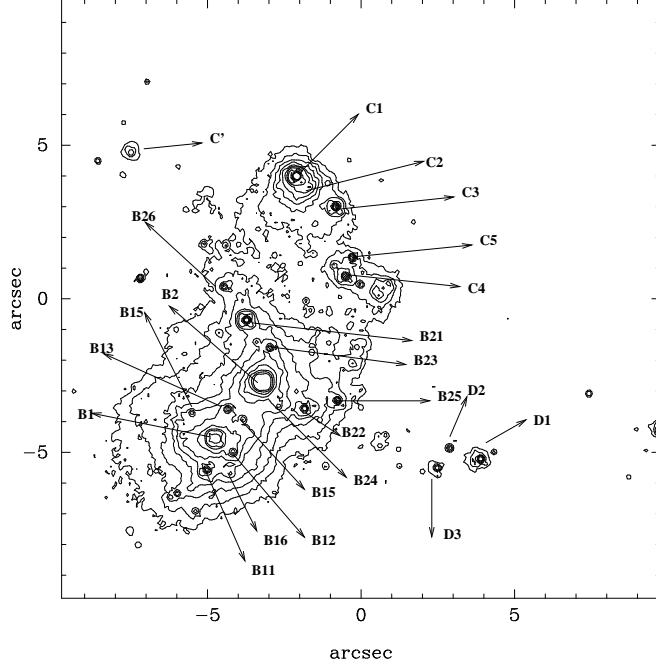


FIG. 7B.— Contour plot on a linear scale of the NIC2 F160W image of NGC 3690. We mark the positions of the B, C and D sources (Table 4). Orientation and field of view as in Figure 7a.

ing the result of Fischer, Smith & Glaccum (1991). The $[\text{Fe II}]1.644\text{ }\mu\text{m}$ and $\text{Pa}\alpha$ images trace the emission from H II regions located in the spiral arms SE of IC 694. The $\text{Pa}\alpha$ emission of the nucleus of IC 694 is similar to the radio H92 α morphology (Zhao et al. 1997). However, the SE emission seen in Zhao et al. (1997) map does not correlate exactly with the $\text{Pa}\alpha$ morphology, possibly due to some obscuration effects at the infrared wavelengths. There are a number of H II regions northwest of B1, and east of C reaching all the way to source C' and extending toward IC 694. In the $\text{Pa}\alpha$ image we can also resolve the B16 source.

The H_2 image of IC 694 shows intense emission from the nucleus of the galaxy together with a beautiful butterfly-like diffuse emission extending over approximately 3 arcsec (see Figure 2.a). The molecular hydrogen image of NGC 3690 shows mainly point-like emission from sources B1, B2 and C, and some diffuse emission from source C' (Figure 2.b).

3.3. Photometry of A, B1, B2, C, and the faint sources

To study the faint sources in Arp 299, we need accurate magnitudes and colors. However, some of these sources, such as the faint objects near B1 and B2, are located on a local background with a substantial gradient. To subtract the contribution of the underlying galaxy, first we extracted subimages of each source, then we produced a two dimensional model of the local background for each source. The source plus background fluxes were fitted unidimensionally along both rows and columns. The source was represented with two Gaussians with different FWHMs and amplitudes, whereas we used a linear fit to the local back-

ground. Although the NICMOS PSF is not perfectly represented by Gaussian functions, the one-dimensional emission profiles were found to be fitted well. The two fits along rows and columns were then averaged together to produce independent 2-D source and the background models. The model background was subsequently subtracted from the original sub-image.

Aperture photometry was done on the background subtracted images. Most of the faint sources appear to be unresolved, so the photometry was obtained through relatively small apertures (typically $0.5''$ in diameter). The final magnitudes and fluxes were corrected for the behavior of the PSF so that the measurement included all the flux associated with a point source. The errors in the photometry for each individual source were computed as the standard deviation of the subimage resulting from the subtraction of the background+source model image from the original image². These errors are approximately 0.1 mag for the faintest sources, decreasing to 0.07 mag for bright ones.

Fluxes (in mJy) measured through the NIC1 F110M, NIC2 F160W, NIC2 F222M and NIC2 F237M filters along with the fluxes (in $\text{erg cm}^{-2} \text{ s}^{-1}$) through the WFPC2 F606W filter are given in Table 4. For the WFPC2 F606W filter we used the photometric calibration from the header of the image, since this filter was not included in the set of WFPC2 calibrated filters. In Table 5 we give the H -band magnitudes and $J - H$, $H - K$ and $R - J$ colors. The $J - H$ and $H - K$ colors were obtained by convolving an empirical galaxy spectral energy distribution with both the NICMOS and J, H, K filter transmission functions and detector response functions. The same convolutions were

² $\sigma_b^2 = \sum \frac{(\text{residual}_{i,j} - \langle \text{residual} \rangle)^2}{n(n-1)}$ with $n = i \times j$ and residual = image - model

TABLE 6
EXTINCTION TO THE GAS FOR THE DIFFERENT COMPONENTS OF ARP 299.

Aperture	source	$f(\text{Pa}\alpha)$ erg cm $^{-2}$ s $^{-1}$	$f(\text{Pa}\alpha)/f(\text{H}\alpha)$	A_V (screen) mag
circular 5''	A	3.7×10^{-13}	1.9	5
	B1	2.3×10^{-13}	0.5	2
	C	4.4×10^{-13}	0.4	2
4.5'' \times 2''	A	3.1×10^{-13}	1.5 – 3.0	4 – 5
	B1	1.7×10^{-13}	0.5 – 1.0	3 – 4
	C	3.3×10^{-13}	0.4 – 0.8	2 – 3
2'' \times 2''	A	2.4×10^{-13}	3 – 5	5 – 6
	B1	1.3×10^{-13}	0.7 – 0.9	3 – 4
	C	2.7×10^{-13}	0.6 – 0.9	3 – 4
Aperture	source	$f(\text{Pa}\alpha)$ erg cm $^{-2}$ s $^{-1}$	$f(\text{Br}\gamma)/f(\text{Pa}\alpha)$	A_V (screen) mag
2.4'' \times 4.7'' ^a	A	3.5×10^{-13}	0.115	24 ± 7
1.2'' \times 1.2''	B1	8.3×10^{-14}	0.102	16 ± 7
	C	1.8×10^{-13}	0.142	37 ± 10
1.1'' \times 2.2'' ^a	B1	9.6×10^{-14}	0.104	17 ± 7
Aperture	source	$f(\text{Pa}\alpha)$ erg cm $^{-2}$ s $^{-1}$	$f(\text{Pa}\alpha)/f(\text{Pa}\beta)$	A_V (screen) mag
2.4'' \times 4.7'' ^b	A	3.5×10^{-13}	5.7	9 ± 2

^aFluxes of Br γ calculated from EW of Br γ and NICMOS continuum calibration (Craig Kulesa private communication).

^bFlux of Pa β calculated from EW of Pa β and NICMOS continuum calibration (Craig Kulesa private communication).

also computed for the galaxy reddened by as much as 40 magnitudes. The convolutions were compared to the values for the standard star P330E in each filter set to derive a transformation between the NICMOS F110M-F160W-F222M system and the *JHK* system. This procedure also corrected for the large color difference between the standard star and our objects in the rather broad F160W filter. The Johnson *R* magnitudes are interpolated between the fluxes at 6060 Å and at 1.10 μ m.

In addition we measure a photometric NICMOS CO index defined as,

$$\text{CO}_{\text{NICMOS}} = \frac{f(\text{F222M}) - f(\text{F237M})}{f(\text{F222M})} \quad (1)$$

This quantity does not formally correspond with the standard photometric CO index, but as Figure 8 illustrates, it is nearly equal to the photometric CO index. The relation plotted in Figure 8 was derived by integrating the SED for an old stellar population across both the two NICMOS filter functions and the ground-based filter functions. The SED was redshifted to .010 and also reddened by amounts ranging from $A_V = 0$ mag to $A_V = 40$ mag. The measured values for both the bright and faint sources are given in Table 5. The NICMOS CO index is subject to the same caveats as the ground-based index because it measures the slope of the continuum between 2.22 μ m and 2.37 μ m as well as the strength of the CO absorption. As we will discuss in Section 3.3.2 it is sensitive to both extinction effects and dilution of the CO bands by hot dust emission.

3.4. Extinction

To interpret the observations requires an accurate estimate of the extinction to each source. The extinction to the gas can be estimated from hydrogen recombination line ratios, so long as the comparison is based on measurements with the same beam sizes. To determine the extinction to the stars one can compare observed colors with the colors of an evolved stellar population. The infrared colors of evolved stellar populations are nearly universal, independent of age. In addition a correction for the dust contribution to the *K*-band fluxes -if any- is required prior to dereddening the stellar colors.

The largest uncertainty in the extinction by far comes from the unknown distribution of dust within the source. Meurer et al. (1995) from their study of the UV properties of starburst galaxies concluded that the dust geometry has to be in a foreground screen configuration near the starburst. However, UV-selected galaxies will be biased toward low extinction and possibly an unrepresentative distribution of the dust. In addition, as emphasized in Section 3.1, the UV may be dominated by non-representative regions within a galaxy. Furthermore, within this study NGC 3690 was a notable exception because it appeared to have patchy extinction. Other authors (e.g., McLeod et al. 1993 for M82; Genzel et al. 1995 for NGC 7469; and Sugai et al. 1999 for Arp 299) find that a simple foreground screen model does not provide a good fit for relatively dust embedded starbursts. They used a model in which dust and gas are homogeneously mixed, and showed that the foreground screen model gives a lower limit – sometimes

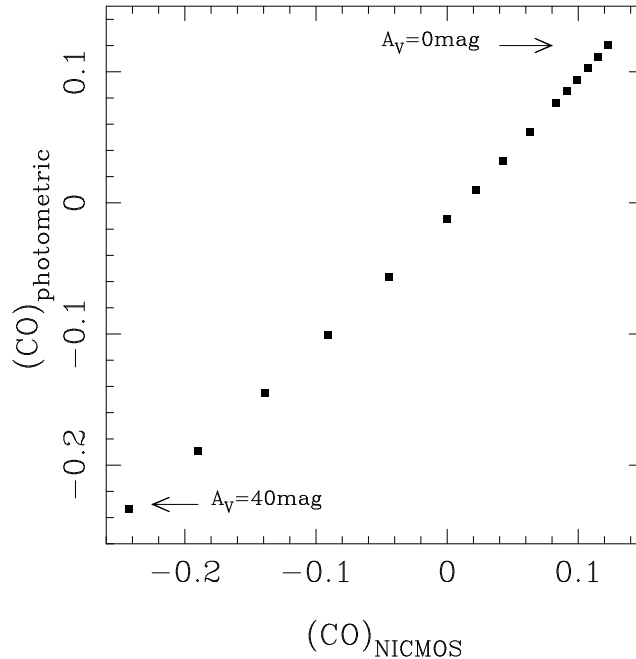


FIG. 8.— Relation between the photometric (CO) index and the $(CO)_{\text{NICMOS}}$ for an elliptical galaxy redshifted to $z = 0.01$ and different values of the extinction from $A_V = 0 \text{ mag}$ through $A_V = 40 \text{ mag}$.

TABLE 7
EXTINCTION TO THE STARS, CORRECTED COLORS AND NICMOS CO
INDICES. DUST EMISSION.

Source (1)	A_V (2)	$(H - K)_{\text{corr}}$ (3)	$CO_{\text{NICMOS}}(\text{corrected})$ (4)	$(f_{\text{dust}}/f_{\text{total}})_K$ (5)
A	6.5	1.01	0.03	...
B1	5.2	1.78	-0.24	...
C1	9.9	1.90	-0.23	...
A	24 ± 7	0.08 ± 0.40	0.15 ± 0.04	0
B1	17 ± 7	1.20 ± 0.40	-0.15 ± 0.04	$\simeq 0.6$
B2	3.5 ± 0.5	0.31 ± 0.03	0.19 ± 0.01	0
C1	37 ± 10	0.43 ± 0.70	0.00 ± 0.06	< 0.2

NOTE.—The errors in columns (3) and (4) take into account the uncertainties associated with the extinction.

by a large factor – to the extinction.

3.4.1. Extinction to the gas

We use a foreground dust screen model and consider its effects on the hydrogen recombination lines. For the infrared extinction law we use a polynomial fit to the A_J , A_H and A_K values given in He et al. (1995). The resulting relative extinctions are, $A(\text{Pa}\beta) = 0.254 \times A_V$, $A(\text{Pa}\alpha) = 0.128 \times A_V$, $A(\text{Br}\gamma) = 0.114 \times A_V$. For the optical lines we use $A(\text{H}\beta) = 1.20 \times A_V$ and $A(\text{H}\alpha) = 0.73 \times A_V$ (Rieke & Lebofsky 1985). The intrinsic values for the Case B hydrogen line ratios are taken from Hummer & Storey (1987) for physical conditions $T_e = 10,000 \text{ K}$ and $n_e = 100 \text{ cm}^{-3}$.

The results for different line ratios and aperture sizes are presented in Table 6. In this table the fluxes of the hydrogen recombination lines are ratioed to the $\text{Pa}\alpha$ flux, which was measured through the corresponding aperture from our NICMOS images. The two values of the $\text{Pa}\alpha$ to $\text{H}\alpha$ ratios and extinctions for the $4.5'' \times 2''$ and $2'' \times 2''$ apertures correspond to the uncertainty of the $\text{H}\alpha$ flux calibration, as discussed in Section 2.3. The results from the $\text{Br}\gamma$ to $\text{Pa}\alpha$ line ratios are presented in the second part of this table. We did not obtain K -band spectroscopy for source A, but we made use of the data in Kulesa et al. (1999). Instead of using their flux calibration, we measured the continuum fluxes from the NICMOS images and used their equivalent widths of $\text{Br}\gamma$ and $\text{Pa}\beta$, to compute the line fluxes. The errors listed in Table 6 for the A_V derived from the $\text{Br}\gamma$ to $\text{Pa}\alpha$ and $\text{Pa}\alpha$ to $\text{Pa}\beta$ line ratios are simply the propagation of the errors in the measured equivalent widths. In Table 3 we give the extinctions derived from the Balmer decrement.

From Table 6 the extinction tends to be higher when line ratios involving longer wavelengths are employed. For instance, the extinction towards source A increases from $A_V = 5.8 \text{ mag}$ from the Balmer decrement up to $A_V = 24 \pm 7 \text{ mag}$ for ratios involving longer wavelengths. A similar trend is found for source C (C1+C2) where extinctions range from $A_V = 2.1 \text{ mag}$ from the optical line ratios (see Table 3) to $A_V = 37 \pm 10 \text{ mag}$ from the $\text{Br}\gamma$ to $\text{Pa}\alpha$ line ratio. The large error of the latter value is due to the small value of the differential extinction between the two lines together with a 10% uncertainty in the flux calibration. From the fluxes of Brackett-series lines given in Sugai et al. (1999) we obtain values of the extinction to source C of between $A_V = 8 \text{ mag}$ and $A_V = 12 \text{ mag}$. For source B1 the extinction does not seem to vary in such a dramatic way, but it still increases toward longer wavelengths, with a maximum value of $A_V = 17 \text{ mag}$.

The differing values as a function of wavelength are the usual indication that the extinction is either patchy or mixed with the emitting sources along the line of sight (or both). In confirmation, for C1+C2 patchy extinction is seen from the optical/near infrared color map (see next section). In addition, our data indicate that the extinction increases for many sources as the aperture is reduced in size. In such a highly-obscured and complex environment we are not probing the same regions in the optical and infrared even when the same aperture sizes are used. This conclusion was already implicit in the differing morphology of the continuum images between these spectral regions (Section 3.1).

The relative distribution of gas and dust appears to be similar for both molecular and ionized hydrogen. Our estimates from near infrared hydrogen recombination lines and a foreground screen are in good agreement with the values derived from the near infrared molecular hydrogen lines and a foreground screen by Kulesa et al. (1999) which are: $A_V = 23 \text{ mag}$ for source A and $A_V = 15 \text{ mag}$ for both sources B1 and C.

3.4.2. Extinction to the stars

We can obtain a qualitative idea about the differential extinction from the color maps presented in Figure 9 (infrared-infrared $H - K$ and optical-infrared $M_{\text{F606W}} - H$). Because the WFPC2 F606W filter contains $\text{H}\alpha$, the optical to near-infrared color maps will show in great contrast bright unobscured HII regions. Both color maps confirm that the extinction to the nucleus of IC 694 is very high. It is interesting that the $H - K$ map shows a similar morphology to the molecular hydrogen emission (the butterfly pattern). The $M_{\text{F606W}} - H$ color map of region C shows patchy extinction with a very red embedded source surrounded by bright HII regions. The ground-based $\text{H}\alpha$ image shows very bright emission from region C, which suggests that the $\text{H}\alpha$ emission is dominated by the bright outer HII regions, whereas the near-infrared recombination lines trace the emission from the very red embedded source. Near B1 we can clearly see the bright HII region associated with source B16, whereas the other sources (B1, and B11 through B15) seem to be obscured by a dust screen, rather than patchy extinction.

A more quantitative estimate of the extinction to the stars can be obtained from the colors. The optical-infrared color $R - J$ is sensitive to age affects and the sources in Arp 299 appear to be young. We therefore use the $J - H$ and $H - K$ colors, which are relatively unaffected by age. As found for the extinction to the gas, when a simple foreground screen model is assumed, the values of the extinction increase from the $J - H$ values to the longer wavelength $H - K$ ones. This effect is shown in the first part of Table 7, where we give the extinction inferred from dereddening $J - H$ to the color of a normal stellar population ($J - H = 0.7$) along with the corrected $H - K$ and $(\text{CO})_{\text{NICMOS}}$ values using that extinction. For the F237M fluxes we interpolated the extinction between the values for A_K and A_L given in Rieke & Lebofsky (1985). The dereddened $H - K$ colors are still very red, but the question remains whether this is the effect of hot dust emission and/or differential extinction. In the second part of Table 7 we give the same quantities but corrected for the highest possible extinction derived from the hydrogen recombination lines.

We can distinguish between these extreme values of the extinction by computing $(\text{CO})_{\text{NICMOS}}$ versus $H - K$ as a function of the properties of any emission by hot dust. Figure 10 shows the results for sources A, B1, B2 and C1. The open star symbols are the values obtained for the extinction derived from the observed $J - H$ color, whereas the filled star symbols are the values obtained using the highest extinction derived from the hydrogen recombination lines. The solid lines represent mixing curves of a normal stellar population and hot dust with different temperatures. For the normal stellar population we integrate the spectrum of an elliptical galaxy redshifted to $z = 0.01$

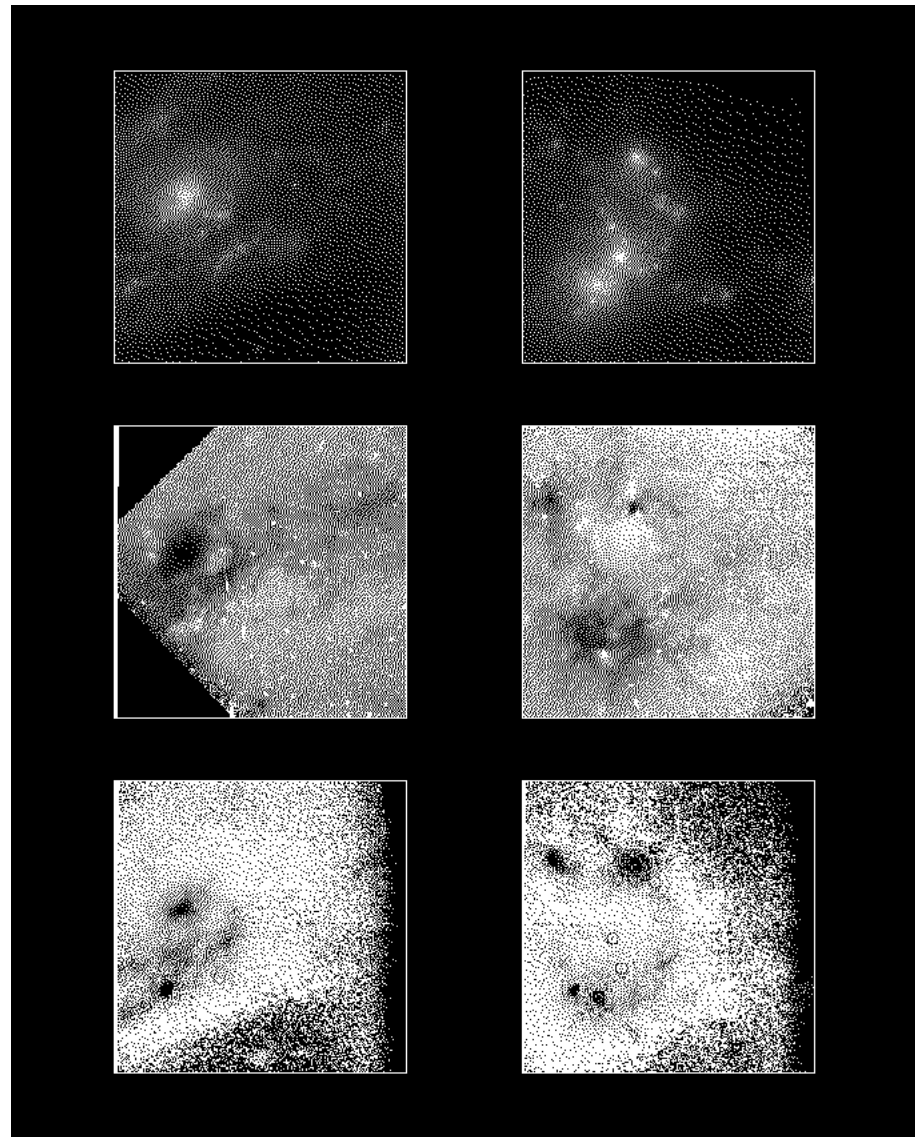


FIG. 9.— The left panels are IC 694 and the right panels are NGC 3690. From top to bottom, H -band images, the WFPC2 F606W / NIC2 F160W color maps (middle) and the NIC2 $H - K$ color maps. Orientation north up, east to the left. The field of view of all the images is $19.5'' \times 19.5''$.

using the filter transmission curves and detector response functions.

The $H - K$ and $(\text{CO})_{\text{NICMOS}}$ values were obtained comparing to the values for the standard star P330E as described in Section 3.3. For the redshifted elliptical galaxy we obtain $H - K = 0.23$ and $(\text{CO})_{\text{NICMOS}} = 0.13$. The dashed lines are the locii of the ratio $(f_{\text{dust}}/f_{\text{total}})_K$ with values 0.2, 0.4, 0.6, 0.8 and 1. These mixing curves are computed by adding different dust contributions (in the form of a blackbody) to the elliptical galaxy. Figure 10 shows that reproducing the $(\text{CO})_{\text{NICMOS}}$ indices and the $H - K$ colors with the extinction obtained by dereddening the $J - H$ colors would require dust temperatures higher than $T = 1000$ K for all sources. Such behavior is atypical of starbursts (e.g., Rieke et al. 1993).

An independent approach to the same issue can be found in Satyapal et al. (1999). They use measurements of the $3.29\mu\text{m}$ PAH emission feature and a standard ratio of feature strength to hot dust continuum to conclude that hot dust can contribute only 7, 3, and 12% respectively to the K-band fluxes of sources A, B, and C.

The other possibility is that there is differential extinction to the stars, as we have already found for the gas. Using the highest values for the gas extinctions (Table 6), we obtain more reasonable temperatures for the dust together with a smaller dust contribution to the K -band flux. Indeed, only source B1 needs a dust contribution of the order of 40%, whereas the other sources require $(f_{\text{dust}}/f_{\text{total}})_K < 0.2$. The fact that using the highest extinctions derived for the gas does produce reasonable values for the dereddened values of $H - K$ and $(\text{CO})_{\text{NICMOS}}$ suggests that the extinction to the gas and to the stars is similar (at least in the near-infrared). The general tendency for the extinction in the gas to be about two times higher than that to the stars (e.g., Calzetti, Kinney, & Storchi-Bergmann 1994) does not appear to hold for this galaxy.

A more realistic approach to the treatment of the extinction should include a model in which stars and dust are mixed (e.g., Witt, Thronson, & Capuano 1992; Witt & Gordon 1999). We used the recently published models of Witt & Gordon (1999) to evaluate the extinction to source A. We find that the $H - K$ color excess can be only reproduced with their shell models, using a K -band extinction of $A_K \simeq 1.8$. This is equivalent to the value used to deredden the K -band magnitude of component A when using the dust screen model (see Section 4.5), confirming the assumption that the system becomes roughly optically thin near the K -band. Note that in Witt & Gordon (1999) models, the relation between A_K and A_V is model dependent.

Finally since $(f_{\text{dust}}/f_{\text{total}})_K$ for source C appears to be relatively small, the lack of CO bands is not due to dilution by hot dust emission, but rather due to the youth of the stellar population that dominates the K -band light. This conclusion is confirmed by the lack of CO bands in the H -band also (see spectrum in Vanzi et al. 1998).

4. STAR FORMATION PROPERTIES

We can distinguish at least six star forming environments in the Arp 299 system: 1.) Component A, the nu-

cleus of IC 694; 2.) component B1; 3.) B2; 4.) C; 5.) C'; and 6.) additional bright H II regions identified individually in our $\text{Pa}\alpha$ images. In this section we will make use of evolutionary synthesis models (Rieke et al. 1993; Engelbracht et al. 1996, 1998) and other arguments to study the star formation properties of these regions. We will assume a truncated Salpeter IMF³. Normalized to the same total mass, this IMF is virtually identical to IMF8 found by Rieke et al. (1993) to give a good fit to the starburst properties of M82. We first consider the parameters that allow us to deduce the star forming properties of these sources.

4.1. Luminosity

Since Arp 299 is an infrared luminous galaxy, we can assume that most of the bolometric luminosity is emitted in the infrared. An estimate of the fraction of the total infrared luminosity from each component can be obtained from ground-based mid-infrared observations of the system (Gehrz et al. 1983; Wynn-Williams et al. 1991; Keto et al. 1996). The relative fluxes at $10\mu\text{m}$, $12\mu\text{m}$, $20\mu\text{m}$ and $32\mu\text{m}$ through a $6''$ -diameter aperture for each component are: A = $27\% \rightarrow 35\% \rightarrow 42\% \rightarrow 63\%$, B1 = $55\% \rightarrow 53\% \rightarrow 40\% \rightarrow 30\%$, and C + C' = $17\% \rightarrow 12\% \rightarrow 18\% \rightarrow 7\%$. We show below that about 10% of the total ionizing luminosity is generated in supergiant H II regions that would not be detectable individually in the ground-based data. Hence we can assume that $\simeq 50\%$ of the total infrared luminosity of the system is concentrated at A (a similar fraction was derived by Joy et al. 1989 for mid-infrared and IRAS far-infrared data), $\simeq 27\%$ is concentrated at component B1 (+ B2) of NGC 3690, $\simeq 13\%$ is at C+C' area, and $\simeq 10\%$ in the supergiant H II regions. From the mid-infrared maps of Keto et al. (1996), it can be inferred that most of the emission for the area B1+B2 comes actually from component B1. For our model fitting we will take the bolometric luminosities given in Table 8 as lower limits, to allow for any escaping energy.

4.2. Mass

An estimate of the available mass is useful as an input to the synthesis models. Shier et al. (1996) derived a mass of $5.6 \pm 1.8 \times 10^9 M_{\odot}$ for IC 694 from the velocity dispersion measured for the $2.3\mu\text{m}$ CO band. This mass is in reasonable agreement (but is larger than) the determination from radio emission lines (Zhao et al. 1997). For component B2 of NGC 3690 the dynamical mass inferred by Shier et al. (1996) is $0.6 \times 10^9 M_{\odot}$, whereas the shallow CO index of B1 did not allow them to get a reliable estimate for this component. We face a similar problem with source C, with its lack of CO bands.

Starburst luminosity varies more slowly than other parameters such as ionizing flux. Since it appears that some of the star forming regions in this system are not in nuclear potential wells, the only useful mass associated with them is the actual mass associated with the local star formation. To estimate the masses of B1 and C where there are no dynamical measurements, we assume the mass-to-light ratio derived for the starburst model of component A, $M/L_{\text{IR}} = 0.004$. The masses of each component are given in Table 8. For B1 we subtracted the dynamical mass of

³ $\phi(m)\text{dm} \propto m^{-2.35}\text{dm}$ between 1 and $80 M_{\odot}$, and $\phi(m)\text{dm} \propto m^{-1}\text{dm}$ between 0.1 and $1 M_{\odot}$.

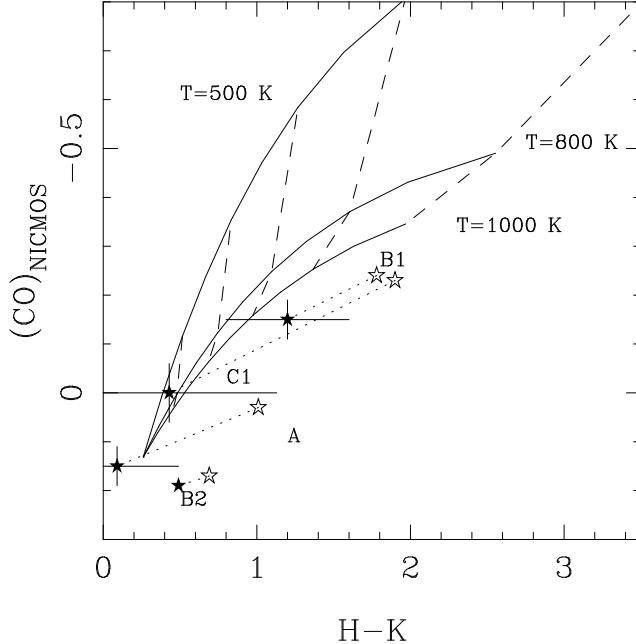


FIG. 10.— $(CO)_{\text{NICMOS}}$ versus $H - K$. The solid lines represent mixing curves of hot dust and a normal stellar population redshifted to $z = 0.010$ ($H - K = 0.23$ and $(CO)_{\text{NICMOS}} = 0.13$), whereas the dashed lines are the fraction of hot dust emission in the K -band: $(f_{\text{dust}}/f_{\text{total}})_K = 0.2, 0.4, 0.6, 0.8$ and 1 (from bottom to top). The open stars are the values for $H - K$ and $(CO)_{\text{NICMOS}}$ corrected for the extinction derived from the $J - H$ color, whereas the filled stars are the values for $H - K$ and $(CO)_{\text{NICMOS}}$ corrected for the (highest) extinction derived from the $\text{Br}\gamma/\text{Pa}\alpha$ line ratio.

B2.

The mass of molecular gas in the interacting system Arp 299 has been estimated from radio CO observations assuming a standard Galactic CO to H_2 conversion (see for instance Sargent & Scoville 1991). These estimates obtain the troubling result that the mass of molecular gas accounts for most of the dynamical mass ($M_{\text{gas}} \simeq 0.7 \times M_{\text{dyn}}$). As discussed by Shier et al. (1994) the standard conversion factor is probably a factor of 3 to 10 too high for infrared luminous galaxies. The work of Shier et al. (1994) has been questioned by Scoville, Yun, & Bryant (1997) and Solomon et al. (1997) on the basis that $2 \mu\text{m}$ spectroscopy will not penetrate the interstellar dust in these systems and hence will underestimate the dynamical mass. However, Zhao et al. (1997) used the $\text{H}92\alpha$ line to measure a dynamical mass for IC 694 less than, but consistent with, that obtained by Shier et al. (1994), supporting the general validity of the arguments of Shier et al. (1994). Braine & Dumke (1998) have recently estimated H_2 masses from the mm-wave thermal emission of interstellar dust in Arp 299 and similar systems and find, in agreement with Shier et al., that the true H_2 masses are probably factors of 3 to 10 lower than given by the standard CO conversion. We therefore assume for all the nuclei that the conversion to $M(\text{H}_2)$ is 30% of the standard value. The molecular mass in A and probably B2 is then about 15% of the total mass, consistent with theoretical expectations for when molecular gas in a galaxy nucleus would tend to break up into star forming clouds (Wada & Habe 1992, Bekki 1995).

4.3. The Number of Ionizing Photons

Zhao et al. (1997) used observations of the radio hydrogen recombination line $\text{H}92\alpha$ to model the physical conditions of the H II regions in components A and B1 of Arp 299. Their modeling has a number of free parameters (such as size of the H II region, electron density, etc). The advantage in using this radio line is that it is not affected by extinction, although the estimated number of ionizing photons is slightly dependent on the model parameters (see Zhao et al. 1997 for a discussion). The resulting uncertainties do not allow them to distinguish between two extreme models involving either a small number (a few tens) of very luminous H II regions with typical sizes of 25 pc, or a large number ($\simeq 10^5$) of modest luminosity H II regions of very compact sizes ($\simeq 0.08$ pc).

The values derived by these authors are $N_{\text{Ly}} = 3.8 - 4.7 \times 10^{54} \text{ s}^{-1}$ for IC 694 (component A). These values correspond to those from the infrared lines if $16 \text{ mag} < A_V < 18 \text{ mag}$. For component B1 of NGC 3690, the fits of Zhao et al. yield $N_{\text{Ly}} = 1.5 - 8.8 \times 10^{53} \text{ s}^{-1}$. The larger value holds for a small number of large H II regions, which is as indicated by our $\text{Pa}\alpha$ imaging and is particularly likely for source B1 because of its compact size in our images. It yields an estimate of $A_V \sim 11 \text{ mag}$.

Within the errors, these extinction values agree with those obtained from the longer wavelength infrared lines. They are significantly larger than would have been deduced from the Balmer decrement or even from the shorter wavelength infrared lines such as $\text{Pa}\beta$ ($\lambda = 1.28 \mu\text{m}$). We adopt values consistent with both the radio and infrared determinations: $A_V = 17 \text{ mag}$ for A and $A_V = 11 \text{ mag}$ for B1. Unfortunately Zhao et al. (1997) did not model component C. From our data and those of Sugai et al. (1999),

we will adopt $A_V = 15$ mag. In general, our arguments regarding the extinction behavior have close quantitative agreement with the work of Sugai et al. (1999). In Table 8 we give the extinction-corrected values for number of ionizing photons (N_{Ly}).

An independent test can be made from the free-free radio continuum. In the case of M82, Puxley et al. (1989) have compared this continuum with the strength of the H 53α line, which is much less subject to modeling uncertainties in converting to N_{Ly} than is H 92α . We therefore have confidence that the strength of the free-free continuum is correctly related to N_{Ly} in M82. By correcting for distance, we predict strengths of 14, 3, and 11 mJy for the free-free emission at 3mm in components A, B, and C, respectively, of Arp 299. The measured fluxes at this wavelength are 17 ± 2 , 5 ± 2 , and 9 ± 2 mJy respectively (Aalto et al. 1997). The agreement is excellent.

For component A, our data, those of Sugai et al. (1999), the comparison with Zhao et al. (1997), and the free-free radio flux are in excellent agreement but strongly disagree with the recent conclusion by Satyapal et al. (1999). The latter reference uses an extinction of only $A_V = 6$ and deduces that the Lyman continuum flux is three times smaller than obtained by the other four approaches. Satyapal et al. acknowledge the discrepancy with the H 92α flux, but they adopt the smaller ionizing fluxes suggested by their extinction levels for their modeling. Since our improved infrared data agree with the higher extinction levels, we believe their values are underestimated due to their use of Pa β in the extinction estimate. Evidently, optical depth effects at $1.28\mu\text{m}$ are significant. Satyapal et al. adopted $A_V = 2$ mag for component C, whereas both our data and those of Sugai et al. indicate a much larger value, $A_V > 10$ mag. The resulting underestimation of the ionizing fluxes undermines the modeling of Satyapal et al. (1999) for these components.

Although for simplicity we (and Satyapal et al.) have used a foreground screen model for the extinction, the agreement with Zhao et al. (1997) is only achieved with the 'high' extinction values from the long wavelength recombination lines. This behavior demonstrates that the dust and gas (and probably the stars) are mixed, and that the system becomes roughly optically thin near the K -band.

4.4. The Supernova Rate

The supernova rate in starburst galaxies can be estimated from radio observations (assuming that the non-thermal radio flux is synchrotron emission produced in shocks associated with supernovae), and from near-infrared [Fe II] emission lines using the calibration obtained for the starburst galaxy M82 (Vanzi & Rieke 1997; Alonso-Herrero et al. 1999). Using the 20 cm radio data of Gehrz et al. (1983) for the apertures which most closely match ours, and the relation between 5 GHz flux density and supernova rate measured for M82 by Huang et al. (1994), we obtain rates of 0.42, 0.11, and 0.06 yr^{-1} for sources A, B, and C respectively. The Condon & Yin (1990) calibration for the supernova rate from Galactic supernovae yields similar values. However, the radio spectrum of source A is too flat near 20 cm to match typical supernovae; we believe it is affected by free-free absorption as previously found for M82 (Rieke et al. 1980). We use the relative nu-

clear flux densities at 8.3 GHz from Zhao et al. (1997) to correct for this effect. We arrive at a best estimate of the supernova rates of 0.65, 0.11, and 0.06 yr^{-1} , respectively. All of these values may be slightly high because free-free emission is expected to contribute at the $\sim 10\text{-}20\%$ level to the observed radio fluxes.

We can also use the newly determined calibration between the [Fe II] $1.644\mu\text{m}$ luminosity and the supernova rate for M82 (Alonso-Herrero et al. 1999), which gives about a two times lower supernova rate than the previous best calibration (Vanzi & Rieke 1997). Correcting the observed [Fe II] fluxes for the appropriate extinctions, we derive supernova rates of 0.52, 0.06 and 0.06 yr^{-1} for A, B1 and C (extinction $A = 15$ mag) in apertures of $2.4'' \times 4.6''$, $1.2'' \times 1.2''$, and $1.2'' \times 1.2''$. The agreement with the radio-based estimate is quite good; for the model fitting we use the radio results, but there would be no change if we had used [Fe II].

4.5. Results from the evolutionary synthesis models

We can interpret the starburst properties with evolutionary synthesis models. The observables that we will try to reproduce with these models are the bolometric luminosity L_{bol} , the K -band luminosity, the number of ionizing photons, the CO index, the supernova rate and the EW of Pa α . The apertures for all the parameters are matched to the infrared spectroscopy. As in Rieke et al. (1993) we normalize the output of the evolutionary synthesis models to the observed values for each component; we will plot the evolution in time of the six quantities so that our target quantity will be unity. The mass-to-light ratios for both K -band luminosity and the bolometric luminosity given in Engelbracht et al. (1996) are used to estimate the contributions of the old underlying population to the total K band and bolometric luminosities. For simplicity, we assume a single burst of star formation with a Gaussian FWHM of 5×10^6 yr. The peak of star formation occurs at 5×10^6 yr after the beginning of the burst.

Source A.

We assume an extinction of $A_V = 17$ mag. The K band luminosity and the N_{Ly} are corrected for extinction using a foreground dust screen. Because we find that the source becomes roughly optically thin at K , this procedure should give reasonably accurate results. For the CO index, we take the value from Shier et al. (1994), which is measured spectroscopically and can be converted accurately to the photometric index used in the models. The fit for the observables of source A (Figure 11.a) uses a total mass in newly formed stars of $7 \times 10^8 M_\odot$ ($\simeq 12\%$ of the dynamical mass) and yields an age for the star formation episode of $6 - 8 \times 10^6$ yr (after the peak of star formation). There is a modest discrepancy in the supernova rate. Measured from the rising half power of the assumed Gaussian in the star formation rate, the age of the burst is then ~ 11 Myr.

Source B1

For the assumed level of the extinction ($A_V = 11$ mag), the contribution of hot dust emission to the observed K luminosity is $(f_{\text{dust}}/f_{\text{total}})_K \simeq 0.5$, which needs to be subtracted to get the stellar K -band luminosity. The observed CO index and equivalent width of Pa α also need to be corrected for the dust emission contribution to the continuum.

TABLE 8
PROPERTIES OF THE COMPONENTS OF ARP 299.

Source	Mass (M_{\odot})	A_V (mag)	L_{IR} (s^{-1})	$N_{\text{Ly}}(\text{total})$ (s^{-1})	K (mag)	CO	SNr (yr^{-1})	EW($\text{Pa}\alpha$) (\AA)
(1)	(2)	(3)	(4)	(5)	(6)	(7)	(8)	(9)
A	5.8×10^9	17	2.5×10^{11}	4×10^{54}	-23.87	0.17	0.65	220
B1	$> 0.4 \times 10^9$	11	$< 1.4 \times 10^{11}$	9×10^{53}	-22.64	-0.15	0.12	100
B2	0.6×10^9	3.5	-	-	-21.76	0.19	-	-
C	$> 0.2 \times 10^9$	15	0.5×10^{11}	3×10^{54}	-22.71	0.00	0.06	500
C'	$> 0.1 \times 10^9$	10	0.25×10^{11}	3×10^{53}	-18.98	-	0.03	1500
SG H II	$\sim 0.02 \times 10^9$	-	0.2×10^{11}	$> 2.2 \times 10^{53}$	-	-	-	-

NOTE.—(1) SG H II represents the sum of the contributions from the 19 most luminous HII regions in the system. No extinction corrections have been applied for them. (2) Dynamical mass for A and B1 from Shier et al. (1996). Masses for remaining components represent forming stellar mass to produce observed infrared luminosity. (3) Assumed foreground extinction level. (4) Estimated infrared (8–1000 μm) luminosity for each component. (5) Total number of ionizing photons corrected for extinction. (6) Extinction corrected K -band absolute magnitude for the small apertures ($2.4'' \times 4.6''$ for Source A, $1.2'' \times 1.2''$ for B1 and C, $2'' \times 2''$ for C'). (7) NICMOS CO index. (8) Supernova rate for small apertures from radio. (9) Equivalent width of $\text{Pa}\alpha$ for the small apertures.

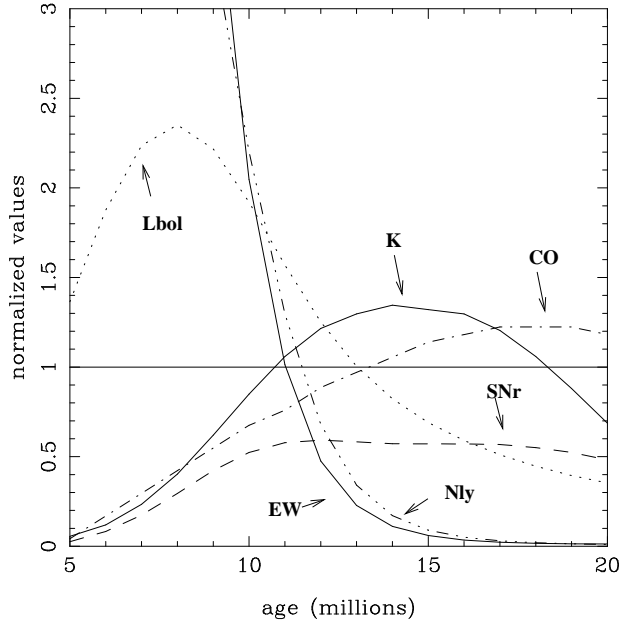


FIG. 11A.— Evolutionary synthesis model fit for source A and a truncated Salpeter IMF. The extinction to the gas is assumed to be the same as the extinction to the stars, $A_V = 17$ mag. The curves are as follows. Solid line (declining) the EW of $\text{Pa}\alpha$. Solid line K -band luminosity. Dotted line the bolometric luminosity. The dashed line the supernova rate. The dot-dot-dot-dash line the CO index. The dot-dot-dot-dash line the number of ionizing photons.

TABLE 9
SYNTHESIS FIT TO C'.

	L_{IR} (L_{\odot})	$N_{\text{Ly}}(\text{total})$ (s^{-1})	K (mag)	SNr (yr^{-1})
(1)	(2)	(3)	(4)	(5)
Observations	0.25×10^{11}	3×10^{53}	-18.98	0.03
Model	0.3×10^{11}	4×10^{53}	-19.0	0.025

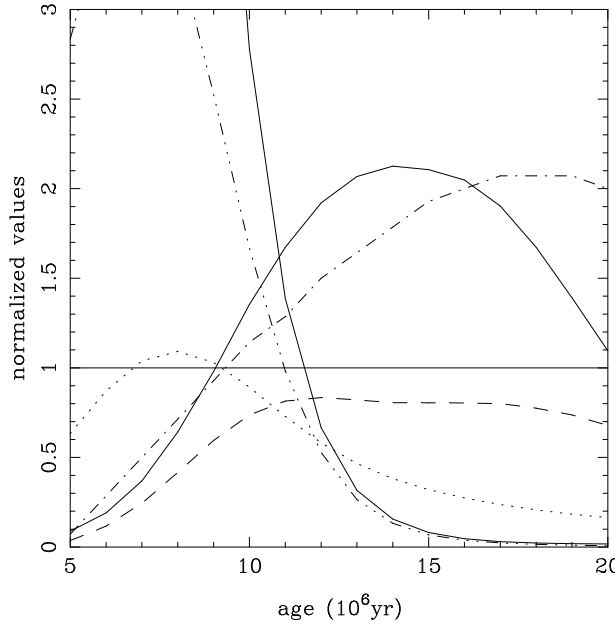


FIG. 11B.— Evolutionary synthesis model fit for source B1 and a truncated Salpeter IMF. The extinction is assumed to be $A_V = 11$ mag.

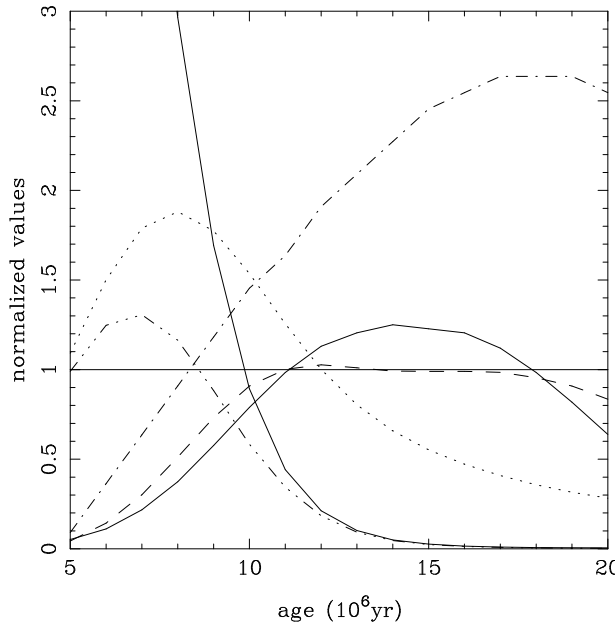


FIG. 11C.— Evolutionary synthesis model fit for source C and a truncated Salpeter IMF. The extinction to the gas is assumed to be the same as the extinction to the stars, $A_V = 15$ mag.

We assume that approximately 70% of the bolometric luminosity of B1+B2 corresponds to B1. The best fit for source B1 is presented in Figure 11.b. The observed values are well fitted at an age between 4.5 and 7 Myr after the peak of star formation. The weak CO absorption suggests an age near the lower end of this range, ~ 5 Myr after the peak, or ~ 7.5 Myr from the rising half power of the assumed Gaussian in the star formation rate.

Source C

Sugai et al. (1999) detect the $1.70\mu\text{m}$ He I line at about 30% the strength of Br 10. Thus, the ionizing flux from this region is dominated by stars with temperatures above 40,000 K (Vanzi et al. 1996). We have already noted the lack of first overtone CO bands from red giant and supergiant stars. Together, these observations require that the starburst in this component be extremely young, dominated by hot stars which have not yet evolved significantly into the red supergiant phase. However, the presence of significant supernova activity, as shown both by the [Fe II] emission and nonthermal radio flux, places a strong lower limit of ~ 3.5 Myr on the age of the starburst.

As a first case for synthesis modeling, we consider a value for the extinction to the gas and to the stars of $A_V = 15$ mag. From Figure 10 we get that $(f_{\text{dust}}/f_{\text{total}})_K \simeq 0.5$. Again the observed CO index (value taken from Ridgway et al. 1994 and the conversion from Doyon et al. 1994 as above) and the equivalent width of Pa α are corrected for the dust contribution to the continuum. The best fit for the truncated Salpeter IMF is presented in Figure 11.c. It corresponds to between 3 and 6 Myr after the peak of star formation. Only the younger of these ages appears possible given the evidence of extreme youth from the He I line. The age after the rising half power point in star formation is then ~ 6 Myr.

Alternately, we can correct the observables for the highest possible extinction obtained from the near-infrared spectroscopy $A_V = 37$ mag (the dust emission contribution to the K -band is less than 20% and the SNr given in Table 8 needs to be increased). We have to assume that 85% of the total bolometric luminosity is unaccounted for in the observed total infrared luminosity, which argues against this high value of extinction. The age derived is even younger than for the previous fit.

Source C'

Component C' presents a dilemma. Its radio spectrum is nonthermal (Baan & Haschick 1990) and its flux density is about 50% of that of component C. However, it is very faint in the near infrared. Our starburst models (Figure 11) assume a Gaussian time dependence with a FWHM of 5 Myr and the supernova rate leads the $2\mu\text{m}$ flux only slightly. However, as the model ages, the $2\mu\text{m}$ flux will persist, so the only time to fit the properties of component C' is during the initial period. To achieve a large ratio of radio to near infrared flux requires that the star formation episode be much shorter in duration than 5 Myr. Rather than reconfigure our starburst program for an instantaneous burst, we use Leitherer & Heckman (1995). Their calculations show that, in such a burst, the supernovae reach their typical level abruptly starting at 3.5 Myr after the burst, while the red supergiants only begin to appear at about 4.5 Myr after the burst. Component C' appears to be adequately explained, then, by a burst of nominally $\sim 3 \times 10^7 M_\odot$ with an age of 4 Myr. The excellent fit

achieved is summarized in Table 9.

It is often found that nuclear starbursts can only be fitted assuming vigorous star formation over 5-10 Myr, as we indicated in this work for component A and as studied in detail for M82 by Rieke et al. (1993) and Satyapal et al. (1997). It is interesting to discover for component C', a region of similar luminosity but not in a potential well, that a very short duration event is required. A similar situation may hold for component C and possibly for B1 (if it is not the second galaxy nucleus), but they are not at the exact stage in their evolution that allows us to draw such a conclusion.

4.6. Other Star Forming Components

Source B2

In addition to these four sources, we deduce that B2 is the site of recent star formation because of: 1.) its strong CO absorption (this work); 2.) its mid infrared excess (Gehr茨 et al. 1983; Keto et al. 1997); and 3.) its nonthermal radio emission (Gehr茨 et al. 1983, Zhao et al. 1997). We can put a lower limit of ~ 11 Myr on the age of this incident because of the very strong CO absorption feature, similar in depth to that of source A. As can be seen from Figure 11, the supernova rate for a given stellar population remains nearly constant from an age of ~ 6 Myr to > 15 Myr. Scaling by the radio emission, we conclude that about $3 \times 10^7 M_\odot$ must have been converted into stars in B2.

Supergiant HII Regions

Our Pa α images reveal a large number of extremely luminous H II regions outside the components listed above. We have no way to correct the Pa α luminosities for extinction, so the derived values are lower limits. We have set a lower limit of $\text{Log}(\text{Pa}\alpha \text{ luminosity}) \geq 38.7 \text{ erg s}^{-1}$, implying $\text{Log}(\text{H}\alpha \text{ luminosity}) \geq 39.7 \text{ erg s}^{-1}$, equivalent to the ionizing luminosity of 30 Doradus. We have located 19 H II regions in the Arp 299 system above this limit. Although we cannot model these regions in detail, we can use the evolutionary models to estimate roughly that each of them involves $\sim 10^6 M_\odot$ of recently formed stars, if the stars form according to the truncated Salpeter IMF and the regions are young.

We can compare this result with the study of 30 nearby galaxies in the H α line by Kennicutt, Edgar, & Hodge (1989). Our method of extracting ionizing line fluxes should give values systematically similar or perhaps lower than used in that work (Kennicutt, private communication). They show that the presence of even one or two H II regions at the 30 Dor level is uncommon in normal galaxies. Although they find that the incidence of supergiant H II regions increases for distorted and interacting galaxies, the extreme number of such objects in Arp 299 is remarkable.

Zhao et al. (1997) called attention to a region with bright H92 α extending to the SE of component A. To a significant extent, this feature appears to be resolved by the NICMOS images into a few supergiant regions. However, the orientation of the feature in the radio maps indicates there may be additional emission in less spectacular condensations.

Massive Stellar Clusters

Much of the past star formation in Arp 299 appears to have been organized into luminous clusters, similar to those

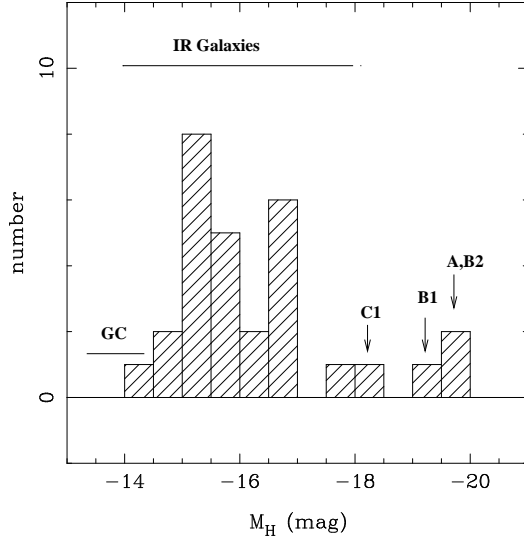


FIG. 12.— Histogram of the absolute H -band magnitudes of the faint sources detected in Arp 299 (not corrected for extinction). Also shown the range of H -band magnitudes for globular clusters and other IR luminous galaxies.

found in other interacting and highly luminous infrared galaxies. The absolute H -band magnitudes for the clusters in Arp 299 (not corrected for extinction) range up to $M_H = -17$ mag (see histogram in Figure 12). This distribution does not include most of the low-luminosity sources, since those were not detected in the NIC1 F110M image. We can compare with the young stellar clusters found in the Antennae, $M_H = -11$ mag to $M_H = -16$ mag (Whitmore & Schweizer 1995) assuming $V - H \simeq 2$. The derived sizes for the stellar clusters in the Antennae are 12 pc (for $H_0 = 75 \text{ km s}^{-1} \text{ Mpc}^{-1}$, Whitmore & Schweizer 1995), whereas our diffraction limit at $1.1 \mu\text{m}$ is approximately 18 pc. In the merger galaxy NGC 7252 young clusters range from $M_H = -16$ mag to $M_H = -18$ mag (Whitmore et al. 1993). The luminosities of the stellar clusters in other infrared luminous and ultraluminous galaxies (Scoville et al. 1999) are also similar to those in Arp 299. However, it should be noted that the ULIRGs in Scoville et al. (1999) paper are more distant than Arp 299, and despite the similarities in H -band luminosities, we may be probing different spatial resolutions.

The cluster luminosities in these extreme galaxies may exceed the limits found in more normal conditions. For example, the intermediate-aged clusters in M100 (Ryder & Knapen 1999) have $M_H = -12$ mag to $M_H = -15$ mag assuming $(H - K \simeq 0.2)$. Since the infrared luminosities change only slowly (see Figure 11), we can compare directly to see that these values may be about 2 magnitudes lower than for ultraluminous galaxies. Further data are needed to confirm this trend.

A crude estimate of the masses of the stellar clusters in Arp 299 can be obtained using the evolutionary synthesis models presented in the preceding section. Although at ages > 25 Myr, the luminosity will fade, it seems unlikely that the clusters in Arp 299 are significantly older than this value, given the young ages derived for the rest of the star formation. In Figure 13 (*left panel*) we present a color-magnitude diagram (absolute H -band magnitude versus the $(H - K)$ color) for the stellar clusters, not cor-

rected for extinction. The lines are the output of models with a truncated Salpeter IMF and masses of $1.5 \times 10^5 M_\odot$, $7.5 \times 10^5 M_\odot$, and $5 \times 10^6 M_\odot$. The peak of the M_H magnitude on each curve corresponds to an age of 10^7 yr, the age at which the red supergiants make the largest contribution. The evolution is shown from 1×10^6 yr up to 5×10^7 yr. The star-symbols are values for the stellar clusters. The errors are 0.15 mag in the colors, and 0.1 mag in the absolute magnitude, and represent the uncertainties associated with the subtraction of the underlying galaxy (Section 3.2). Most of the stellar clusters lie to the right of the model predictions indicating that some extinction is present.

From Table 5 it is clear that most of the stellar clusters do not show extremely red colors as it is the case of the bright nuclei A, B1, B2 and C1. However the observed colors are still redder than the values predicted by the model. The predictions of the model show variations in the $J - H$ color of less than 0.1 mag around $J - H = 0.7$ for ages $> 10^7$ yr. Since the ages of the clusters are expected to be greater than 10^7 yr, one can use the observed $J - H$ color to obtain an estimate of the foreground extinction. We find that the extinctions are typically $A_V = 1.7 - 4$ mag, much lower than the extinction to the bright sources. Figure 13 (*right panel*) shows how the values of M_H and $(H - K)$ corrected for extinction lie closer to the model predictions, although they are still somewhat redder. The masses of these clusters are in the range of $1.5 \times 10^5 - 5 \times 10^6 M_\odot$. For comparison the masses of the stellar clusters found in other infrared luminous galaxies are $10^5 - 10^7 M_\odot$ (Scoville et al. 1999), whereas the masses of Galactic globular clusters are of the order of $10^5 M_\odot$ (van der Bergh 1995).

Given the modest extinctions to the clusters, their deep CO bands (see Table 5) require little correction. Assuming roughly solar metallicity, these band strengths can only be produced by stellar populations of age $\sim 10\text{-}30$ Myr.

4.7. An Extended Period of Elevated Star Formation

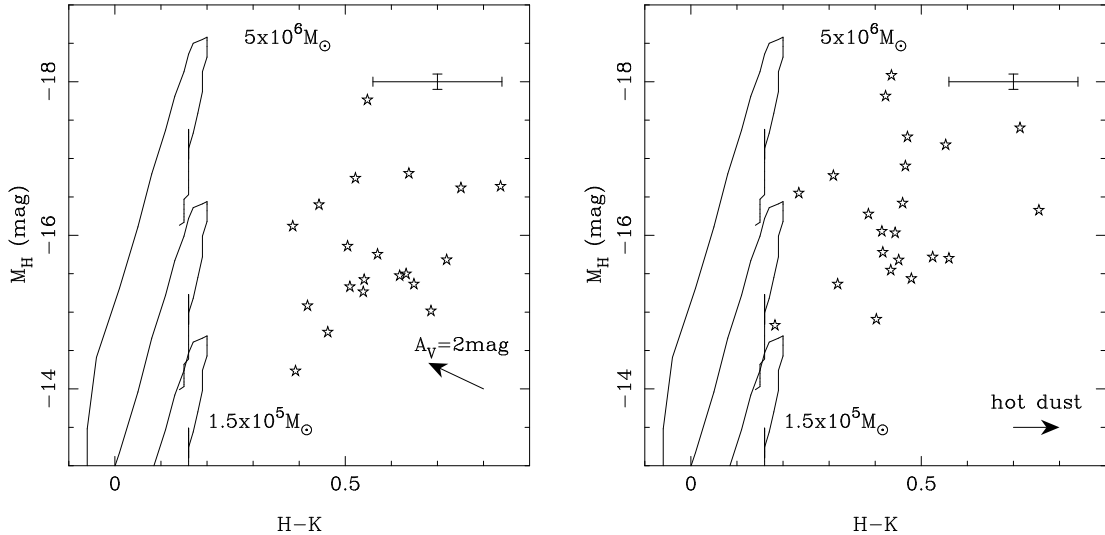


FIG. 13.— *Left panel* Absolute H -band magnitude versus $(H - K)$ for the stellar clusters, not corrected for extinction. The lines are the output of models using a truncated Salpeter IMF, and cluster masses of $1.5 \times 10^5 M_{\odot}$, $7.5 \times 10^5 M_{\odot}$, and $5 \times 10^6 M_{\odot}$. *Right panel* Same but using colors and magnitudes corrected for extinction. The error bars are indicated in the upper right corners of the plots.

The major starforming components in Arp 299 show a large range of ages. Even though some uncertainties remain regarding the ages and burst strengths, we find an age gradient from B2 (> 11 Myr) to A (~ 11 Myr) to B1 (~ 7.5 Myr), C (~ 5 Myr), and C' (4 Myr). Compared with Satyapal et al. (1999), we derive an older age for source A, assuming that its starburst has had a relatively long duration (they assumed an instantaneous burst), a similar age for source C, and we resolve source B into two bursts of differing ages, one older than and the other younger than their value. The effective star formation rate (mass of the newly formed stars over the FWHM of the burst) is high for component A ($140 M_{\odot} \text{ yr}^{-1}$). It is moderately high also for B1 ($40 M_{\odot} \text{ yr}^{-1}$) and for C ($22 M_{\odot} \text{ yr}^{-1}$) (or $120 M_{\odot} \text{ yr}^{-1}$ if the extinction to C is as high as 37 magnitudes). The masses in newly formed stars are about $7 \times 10^8 M_{\odot}$ for component A, about $1 \times 10^8 M_{\odot}$ for B1, $1 \times 10^8 M_{\odot}$ for C, $1 \times 10^8 M_{\odot}$ for C', and $0.3 \times 10^8 M_{\odot}$ for B2.

We find a similar range for star formation in very massive stellar clusters. We have identified 19 supergiant H II regions, and have deduced total stellar masses for them that are similar to the masses of 21 stellar clusters with $-15 > M_H > -17$. The H II regions must be young, 5 Myr or less, whereas the strong CO absorption in the clusters implies typical ages > 10 Myr.

Star formation has been occurring contemporaneously throughout the two galaxies over the past 10-15 Myr, both within and outside of their nuclei. There appear to be four potentially differing environments for the star formation. Outside of the nuclei and along the spiral arms, there are massive stellar clusters and H II regions. Within the nuclear potential wells, young stars have formed in numbers one to two orders of magnitude greater than in these clus-

ters. Although we cannot be sure of the spatial distribution of star formation in the nuclei now, it is plausible that these populations will merge into a single super-cluster, given the high density of young stars and the strong tidal forces that would cause clusters to disintegrate rapidly. In the interaction region, components C and C' appear to be locations where star formation has occurred on the scale typical of a galaxy nucleus, not an extranuclear cluster. Presumably, there is no nuclear potential well in this region, but the concentration of molecular gas in the interaction has resulted in an exceptionally vigorous star formation episode. This is also found in other interacting galaxies (e.g., VV114 Frayer et al. 1999; the Antennae Vigroux et al. 1996). Finally, there may be examples of extreme star formation near the galaxy nuclei where infalling gas clouds became unstable and formed stars before falling all the way into the nuclear potential. One possible example is the region SE of the nucleus of IC 694 (component A) in the H92 α measurements of Zhao et al. (1997) and partially resolved into supergiant H II regions in our data. Another possible example is components B1 and B2. It is not obvious which should be associated with a galaxy nucleus. However, we have found that both involve a larger mass of young stars than can be attributed to a supergiant H II region or massive stellar cluster, so it is plausible to assume one is a galaxy nucleus and the other a very nearby star forming region.

5. FATE OF THE STARBURST REGIONS

Sources B1 & B2

The measure of stellar dynamics in B2 (Shier et al. 1996) suggests a mass of $6 \times 10^8 M_{\odot}$, whereas from the radio luminosity we have found that only about $3 \times 10^7 M_{\odot}$ is expected from recent star formation. Thus, this object

appears to satisfy expectations for a modest mass galaxy nucleus. On the other hand, the ^{12}CO emission is centered on B1 and has a FWHM of 260 km s^{-1} (Aalto et al. 1997), possibly indicating a larger mass there, $\sim 3 \times 10^9 M_\odot$. It is possible that the CO is subject to non-gravitational forces at B1, or that the stellar population at B2 is not gravitationally bound, so the situation of these two nearby concentrations is not firmly determined by the observations.

If B1 has a mass of $3 \times 10^9 M_\odot$, then the Roche radius for B2 is ~ 200 pc, about one third of the projected separation of the sources. In this case, B2 will be undergoing significant tidal evaporation and is in the process of merging into the general stellar distribution around B1. On the other hand, the dynamical mass of B2 is similar to the mass of B1 indicated for the recent star formation. We may be seeing two galaxy nuclei of comparable masses, one older and the other newly formed, orbiting each other at a projected distance 5-6 times the Roche radii. The dynamical evolution will be more complex in this situation and should develop more slowly, but will probably have a similar end point.

Sources C & C'

Sources C and C' are well isolated from the galaxy nuclei in the system - they are about 3 kpc from component A and 1.5 kpc from B, projected onto the sky. They do not appear to lie within any significant potential wells of their own, based on the lack of evidence for an underlying concentration of old, red stars. This case is particularly strong for C', given how faint it is in the near infrared. Both objects have low velocity dispersions in ^{12}CO of $60 - 80 \text{ km s}^{-1}$ (Aalto et al. 1997). Given our estimates of the total mass being converted into stars (Table 8), the low velocity dispersion is consistent with the formation of a bound stellar system. The relaxation time for such a system can be estimated from the expression in Spitzer (1987) to be long, of order 10^{12} yr. Thus, it would appear that C and C' represent the formation of stellar systems on the scale of dwarf galaxies. A further confirmation of this possibility comes from the star formation efficiency. The gas masses of both C and C' are $\sim 3 \times 10^8 M_\odot$ (from the ^{12}CO measurements of Aalto et al. (1997) and our adjusted conversion to H_2 mass, see Section 4.2). The mass of newly formed stars is likely to be $1 \times 10^8 M_\odot$ for both, as indicated in Table 8. Thus, a significant fraction of the molecular material in these regions has probably been turned into stars, a situation that favors formation of bound systems.

The effects of tidal forces on this system can be estimated roughly from the Roche limit, which is about 500 pc relative to the nucleus of IC 694. Therefore, the stellar systems may persist for a significant lifetime, so long as they do not approach more closely to the massive nucleus of IC 694 than at present. They are perhaps best described, given their masses and potential stability, as new dwarf galaxies.

Supergiant HII Regions & Stellar Clusters

Although the giant stellar clusters seen in other starbursts have been described as young globular clusters, the distribution of these objects along spiral arms argues against a literal interpretation of this view. In IC 694, many of these objects lie a few Roche radii from the galaxy nucleus in projected distance. If the larger mass estimate holds for B1 in NGC 3690, a similar situation holds there.

It is therefore plausible that the clusters that lie relatively close to the massive galaxy nuclei will be subject to strong tidal evaporation and will fade in prominence as the massive stars die and the less massive ones are lost into the surrounding galaxies. However, clusters that lie relatively far from nuclear mass concentrations may be reasonably stable.

6. CONCLUSIONS

We have used *HST*/NICMOS broad-band and narrow-band images of Arp 299, along with archival HST data and ground-based spectroscopy and imaging to study this complex system. We find:

- 1.) Arp 299 is dominated by widespread and powerful star formation. In common with other recent studies, we find no evidence for an AGN anywhere in the system.
- 2.) As found for other infrared starburst and luminous and ultraluminous galaxies, the extinction toward the dominant infrared sources is extremely strong and complex. Studies using optical or near infrared measures of extinction (e.g., Satyapal et al. 1999) will significantly underestimate its importance and will deduce erroneous values for the critical parameters characterizing the star forming activity. Studies based only on UV light will face even more severe difficulties.
- 3.) The infrared [Fe II] line emission predicts a rate of supernova activity in close agreement with that from the nonthermal radio fluxes, and both are in satisfactory agreement with the predictions of evolutionary synthesis starburst models.

The detailed morphology of the components of Arp 299 has been revealed with the *HST*/NICMOS broad-band images. The system is a veritable museum of interaction-induced star formation. It includes:

- 1.) A massive galaxy nucleus (IC 694, source A) undergoing an extended-duration starburst and accounting for $3 \times 10^{11} L_\odot$, about 50% of the total luminosity of the system.
- 2.) A strongly star forming region near this nucleus, H92α SE, probably indicating a region where infalling molecular clouds broke up into star forming regions before getting all the way into the nuclear potential well.
- 3.) A pair of sources (NGC 3690, B1 and B2) probably representing a less massive galaxy nucleus and a vigorous star formation episode where molecular clouds became unstable in its vicinity, together representing about $1.5 \times 10^{11} L_\odot$, about 27% of the total.
- 4.) Very young and vigorous star forming regions (C and C') near the interface between the two galaxies. They are likely to be forming gravitationally bound stellar systems that will eventually have the appearance of dwarf galaxies.
- 5.) A numerous population of supergiant H II regions and stellar clusters both near the more powerful star forming regions and along spiral arms. They appear to represent young and old phases of extreme star formation outside the galaxy nuclei.

We have used evolutionary synthesis modeling and other arguments to assign ages to these various manifestations of star formation, finding that they have all persisted for at least 10 – 15 Myr. Thus, Arp 299 has been in a condition similar to what we observe now for about this period of time, with all or nearly all the varieties of star forming environments active.

Arp 299 should be similar to other luminous infrared galaxies. The greater complexity revealed for it is primarily a result of its relative proximity (42 Mpc) and our use of very high resolution near infrared images from NICMOS, giving a physical resolution of about 20 pc.

ACKNOWLEDGMENTS

During the course of this work AA-H was supported by the National Aeronautics and Space Administration on

grant NAG 5-3042 through the University of Arizona. The work was also partially supported by the National Science Foundation under grant AST-95-29190. We are grateful to Kevin Luhman for obtaining the optical spectra presented in this paper, and to Craig Kulesa for providing us with data prior to publication. We thank Karl Gordon andn Chad Engelbracht for helpful discussions.

REFERENCES

Aalto, S., Radford, S. J. E., Scoville, N. Z., & Sargent, A. I. 1997, *ApJL*, 475, L107

Alonso-Herrero, A., Rieke, M. J., & Rieke, G. H. 1998, in NICMOS and the VLT: A New Era of High Resolution Near Infrared Imaging and Spectroscopy, ESO Conference and Workshop Proceedings, ed. Wolfram Freudling and Richard Hook, 55, p.172

Alonso-Herrero, A., Rieke, M. J., Rieke, G. H., & Kelly, D. 1999, *ApJ*, in preparation

Baan, W. A., & Haschick, A. 1990, *ApJ*, 364, 65

Barnes, J. E., & Hernquist, L. 1996, *ApJ*, 471, 115

Bekki, K. 1995, *MNRAS*, 276, 9

Braine, J., & Dumke, M. 1998, *A&A*, 333, 38

Calzetti, D., Kinney, A. L., & Storchi-Bergmann, T. 1994, *ApJ*, 429, 582

Condon, J. J., & Yin, Q. F. 1990, *ApJ*, 357, 97

Doyon, R., Joseph, R. D., & Wright, G. S. 1994, *ApJ*, 421, 101

Engelbracht, C. W., Rieke, M. J., Rieke, G. H., & Latter, W. B. 1996, *ApJ*, 467, 227

Engelbracht, C. W., Rieke, M. J., Rieke, G. H., Kelly, D. M., & Achtermann, J. M. 1998, *ApJ*, 505, 639

Frayer, D. T., Ivison, R. J., Smail, I., Yun, M. S., & Armus, L. 1999, *AJ*, 118, 139

Fischer, J., Smith, H. A., & Glaccum, W. 1991, in *ASP Conf. Ser.* Vol. 14, *Astrophysics with Infrared Arrays*, ed. R. Elston (San Francisco: ASP), 63

Gehrz, R. D., Sramek, R. A., & Weedman, D. W. 1983, *ApJ*, 267, 551

Genzel, R., Weitzel, L., Tacconi-Garman, L. E., Blietz, M., Cameron, M., Krabbe, A., Lutz, D., Sternberg, A. 1995, *ApJ*, 444, 129

He, L., Whittet, D. C. B., Kilkenny, D., Spencer Jones, J. H. 1995, *ApJS*, 101, 335

Ho, L. C., Filippenko, A. V., & Sargent, W. L. 1993, *ApJ*, 417, 63

Huang, Z. P., Thuan, T. X., Chevalier, R. A., Condon, J. J., & Yin, Q. F. 1994, *ApJ*, 424, 114

Hummer, D. G., & Storey, P. J. 1987, *MNRAS*, 224, 801

Kennicutt, R. C., Edgar, B. K., & Hodge, P. W. 1989, *ApJ*, 337, 761

Keto, E., Hora, J. L., Deutsch, L., Hoffman, W., Fazio, G. G., Ball, R., Meixner, M., Skinner, C., Arens, J. F., & Jernigan, G. 1997, *ApJ*, 483, 598

Kleinmann, S. G., & Hall, D. N. B. 1986, *ApJS*, 62, 501

Kulesa, C. A., Black, J. H., Rieke, G. H., & Rieke, M. J. 1999, in preparation

Leitherer, C., & Heckman, T. M. 1995, *ApJS*, 96, 9

McLeod, B. 1997 in *HST Calibration Workshop*, ed. S. Casertano et al.

McLeod, K. K., Rieke, G. H., Rieke, M. J., & Kelly, D. M. 1993, *ApJ*, 412, 111

Meurer, G. R., Heckman, T. M., Leitherer, C., Kinney, A., Robert, C., & Garnett, D. R. 1995, *AJ*, 110, 2665

Oliva, E., & Origlia, L. 1992, *A&A*, 254, 466

Puxley, P. J., Brand, P. W. J. L., Moore, T. J. T., Mountain, C. M., Nakai, N., & Ymamshita, T. 1989, *ApJ*, 345, 163

Ridgway, S. E., Wynn-Williams, C. G., & Becklin, E. E. 1994, *ApJ*, 428, 609

Rieke, G. H., & Low, F. J. 1972, *ApJ*, 176, L95

Rieke, G. H., & Lebofsky, M. J. 1985, *ApJ*, 288, 618

Rieke, G. H., Lebofsky, M. J., Thompson, R. I., Low, F. J., & Tokunaga, A. T. 1980, *ApJ*, 238, 24

Rieke, G. H., Loken, K., Rieke, M. J., & Tamblyn, P. 1993, *ApJ*, 412, 99

Ryder, S. D., & Knapen, J. H. 1999, *MNRAS*, 302, L7

Sanders, D. B., Soifer, B. T., Elias, H. J., Modore, B. F., Mathews, K., Neugebauer, G., & Scoville, N. Z. 1988, *ApJ*, 325, 74

Sanders, D. B., & Mirabel, I. F. 1996, *ARA&A*, 34, 749

Sargent, A., & Scoville, N. 1991, *ApJ*, 366, L1

Satyapal, S., Watson, D. M., Pipher, J. L., Forrest, W. J., Greenhouse, M. A., Smith, H. A., Fischer, J., & Woodward, C. E. 1997, *ApJ*, 483, 148

Satyapal, S., Watson, D. M., Pipher, J. L., Forrest, W. J., Fischer, J., Greenhouse, M. A., Smith, H. A., & Woodward, C. E. 1999, *ApJ*, 516, 704

Scoville, N. Z., Yun, M. S., & Bryant, P. M. 1997, *ApJ*, 484, 702

Scoville, N. Z., Evans, A. S., Dinshaw, N., Thompson, R., Rieke, M., Schneider, G., Low, F. J., Hines, D., & Stobie, B. 1998, *ApJ*, 492, L107

Scoville, N. Z., Evans, A. S., Thompson, R., Rieke, M., Hines, D., Low, F. J., Dinshaw, N., Surace, J. A., & Armus, L. 1999, submitted

Shier, L. M., Rieke, M. J., & Rieke, G. H. 1994, *ApJ*, 433, L9

Shier, L. M., Rieke, M. J., & Rieke, G. H. 1996, *ApJ*, 470, 222

Solomon, P. M., Downes, D., Radford, S. J. E., & Barrett, J. W. 1997, *ApJ*, 478, 144

Spitzer, L. 1987, "Dynamical Evolution of Globular Clusters," (Princeton: Princeton University Press), p.40

Sugai, H., Davies, R. I., Malkan, M. A., McLean, I. S., Usuda, T., & Ward, M. J. 1999, *ApJ*, in press

van der Bergh, S. 1995, *Nature*, 374, 215

Vanzi, L., Rieke, G. H., Martin, C. L., & Shields, J. C. 1996, *ApJ*, 466, 150

Vanzi, L., & Rieke, G. H. 1997, *ApJ*, 479, 694

Vanzi, L., Alonso-Herrero, A., & Rieke, G. H. 1998, *ApJ*, 504, 93

Vigroux, L. et al. 1996, *A&A*, 315, L93

Wada, K., & Habe, A. 1992, *MNRAS*, 258, 82

Whitmore, B. C., Schweizer, F., Leitherer, C., Borne, K., & Robert, C. 1993, *AJ*, 106, 1354

Whitmore, B. C., & Schweizer, F. 1995, *AJ*, 109, 960

Williams, D. M., Thompson, C. L., Rieke, G. H., & Montgomery, E. F. 1993, *Proc. SPIE*, 1946, 482

Witt, A. N., & Gordon, K. D. 1999, *ApJ*, in press

Witt, A. N., Thronson, H. A., & Capuano, J. M. Jr. 1992, *ApJ*, 393, 611

Wynn-Williams, C. G., Eales, S. A., Becklin, E. E., Hodap, K. -W., Joseph, R. D., McLean, I. S., Simons, D. A., & Wright, G. S. 1991, *ApJ*, 377, 426

Zhao, J., Anantharamaiah, K. R., Goss, W. M., & Viallefond, F. 1997, *ApJ*, 482, 186